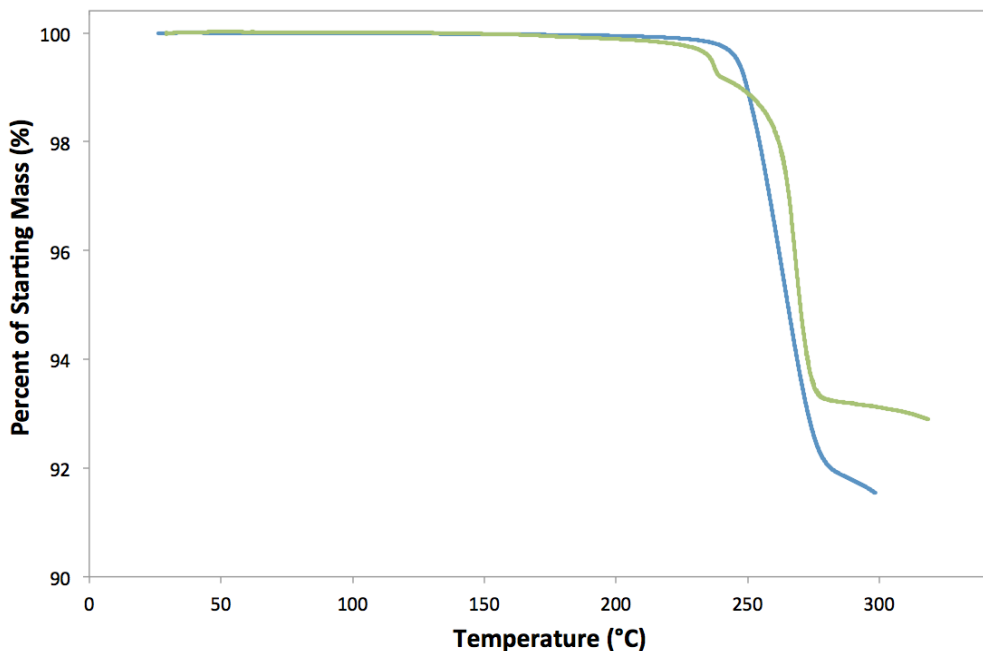


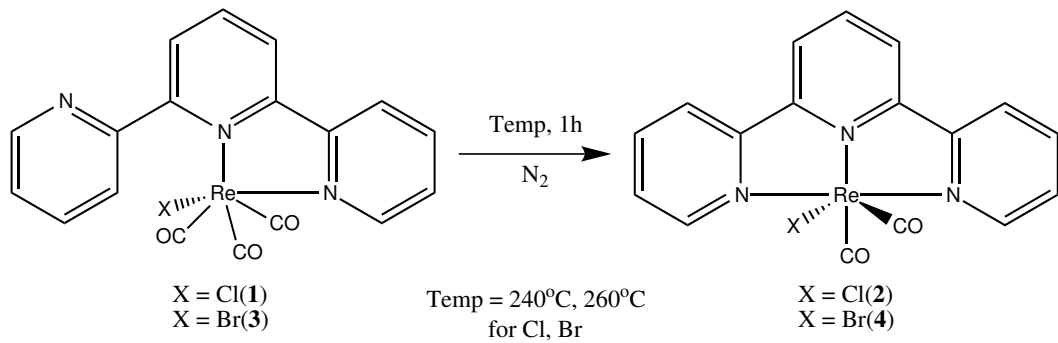
the appropriate thermolysis temperature was performed by Thermogravimetric Analysis (TGA) of the sample. A loss of 6-8 % of starting mass from the sample is consistent with the loss of one carbonyl group from the complex. Results of TGA on **2.1** and **2.3** is shown in Figure 2.1.



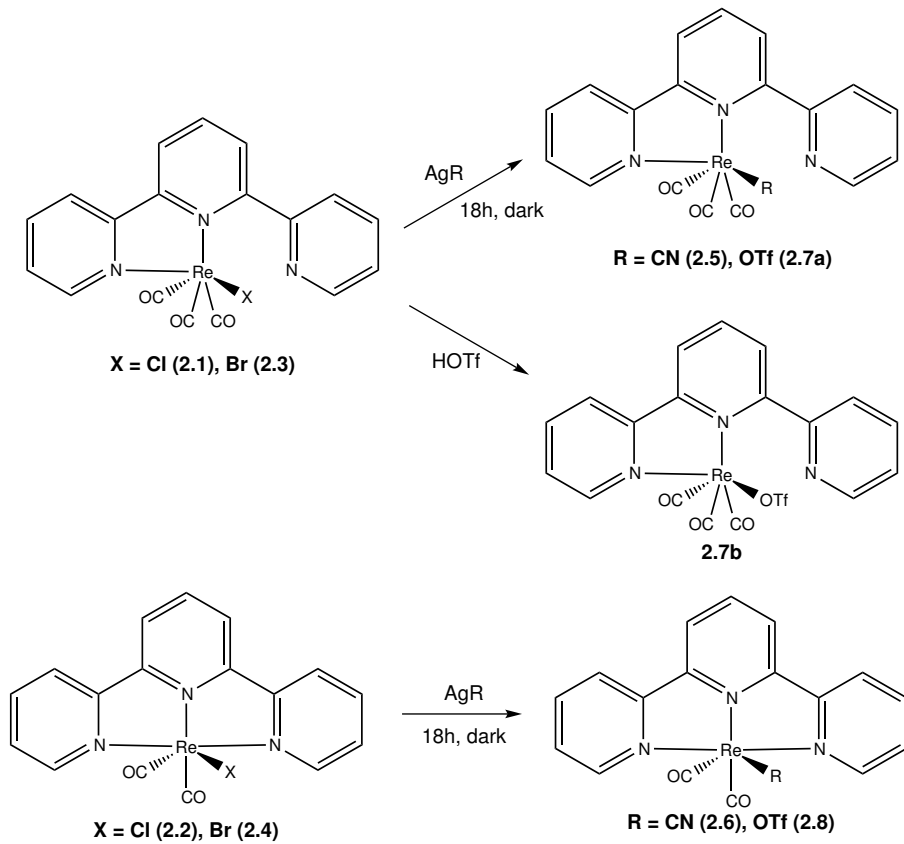
**Figure 2.1** Results of TGA analysis on **2.1** (blue) and **2.3** (green).

The onset of mass loss in the TGA of **2.1**, and the onset of the main mass loss in the TGA of **2.3** were chosen to identify a thermolysis temperature for each sample. For **2.1**, thermolysis was performed at 240 °C, and for **2.3** thermolysis was performed at 260 °C, yielding **2.2** and **2.4** respectively, at quantitative yields, by the pathway in Scheme 2.2.

Further reactions were carried out on the above products to yield triflate and cyano complexes in bidentate and terdentate geometries. These anion exchange reactions were performed by the addition of the silver salt to the chloride products **2.1** or **2.2**, to precipitate AgCl, leaving  $\kappa^2$ (terpy)Re(CO)<sub>3</sub>CN (**2.5**),  $\kappa^3$ (terpy)Re(CO)<sub>2</sub>CN (**2.6**),  $\kappa^2$ (terpy)Re(CO)<sub>3</sub>OTf (**2.7a**) and  $\kappa^3$ (terpy)Re(CO)<sub>2</sub>OTf (**2.8a**), as shown in Scheme 2.3.



**Scheme 2.2** Synthesis of **2.2** and **2.4** by thermolysis of **2.1** or **2.3**, respectively.



**Scheme 2.3** Anion exchange pathways to synthesize **2.5** - **2.8**.

Reaction with the bromide products proceeds with similar results. As the Ag anion exchange reactions result in only moderate yields, **2.7b** was synthesized by the direct

addition of neat triflic acid ( $\text{CF}_3\text{SO}_3\text{H}$ ) to **2.1**. HCl was released, the solutions were quenched by addition of dilute aqueous  $\text{NaCO}_3$ , and product was collected via separation into chloroform, again at moderate yield.

## 2.3 Characterization

Full characterization was performed, including Nuclear Magnetic Resonance (NMR) analysis, x-ray crystallography, elemental analysis, as well as UV-Vis and IR spectroscopy. Computational Density Functional Theory (DFT) methods were used to solve the geometries, and Time Dependant Density Functional Theory (TD-DFT) was performed to predict UV-Vis spectra and identify electronic transitions.

### 2.3.1 NMR Analysis

Proton NMR was performed on each of the samples. Each sample was dissolved completely in deuterated acetonitrile ( $\text{CD}_3\text{CN}$ ) and analysis was performed on a Bruker AVANCE 400 MHz spectrometer. Data was processed from the FID signal via the Top-Spin program, and spectra were analyzed using ACD NMR Processor v12.0.

Detailed peak analysis comparing bidentate samples **2.1**, **2.3**, **2.5**, and **2.7** (Figure 2.2) or terdentate **2.2**, **2.4**, **2.6**, and **2.8** (Figure 2.5) show little difference between samples. This is due to the distance between the anion and any protons on the ligand. Anions with different  $\sigma$ -donor strength marginally impact the metal-ligand interactions; these have only small effect on the location of peaks, shifting between samples by typically less than 0.1 ppm. As is shown in Figure 2.2, the characteristic shape of each spectra remains constant, only exact peak locations and some peak order varies with anion choice.

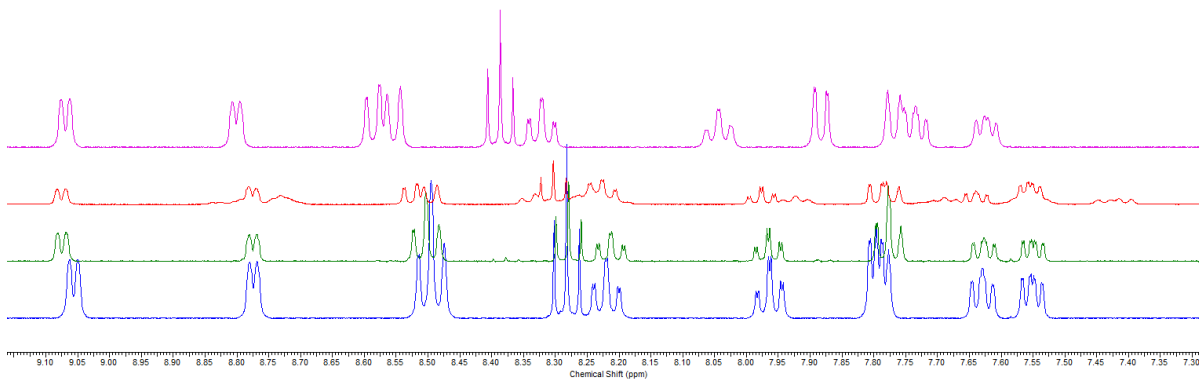


**Figure 2.2** The aromatic region of the <sup>1</sup>H NMR spectra for bidentate compounds **2.1** (blue), **2.3** (green), **2.5** (red) and **2.7** (purple).

The characteristic feature in the NMR spectra after the transformation from bidentate to terdentate (e.g. sample **2.1** to **2.2**) is the reduction in the total number of the signals in the aromatic region (between 7 and 9 ppm). This simplification is due to the increased symmetrization of the ligand, while the  $\kappa^2$ -bidentate ligand has a freely rotating pendant group. Prior work in literature<sup>51</sup> and in our group<sup>128</sup> shows the temperature dependence of the rate of rotation of this pendant arm for various ligand species. However, the  $\kappa^3$ -terdentate species has no free groups, the rigid geometry and higher order symmetry results in the simpler NMR spectrum.

The simplification of peaks due to the symmetrization of the ligand results in the peaks from free pendant arm protons *a*, *b*, *c*, and *d* (see Figure 2.4) with peaks at 9.06, 7.63, 8.22 and 7.79 ppm, respectively, aligning with their mirroring peaks at *a'*, *b'*, *c'* and *d'* (with peaks at 8.77, 7.55, 7.96, and 7.80 ppm). The new symmetrized peaks show integrations of two protons per peak, relative to the single proton (*f*) peak from the central pyridyl ring, *para* to the nitrogen. As well, the presence of metal-ligand interaction in the pendant arms reduces the deshielding effect, shifting the free pyridyl *ortho* proton from 9.06 to 8.77 ppm in the chelated group, with similar shifts evident for

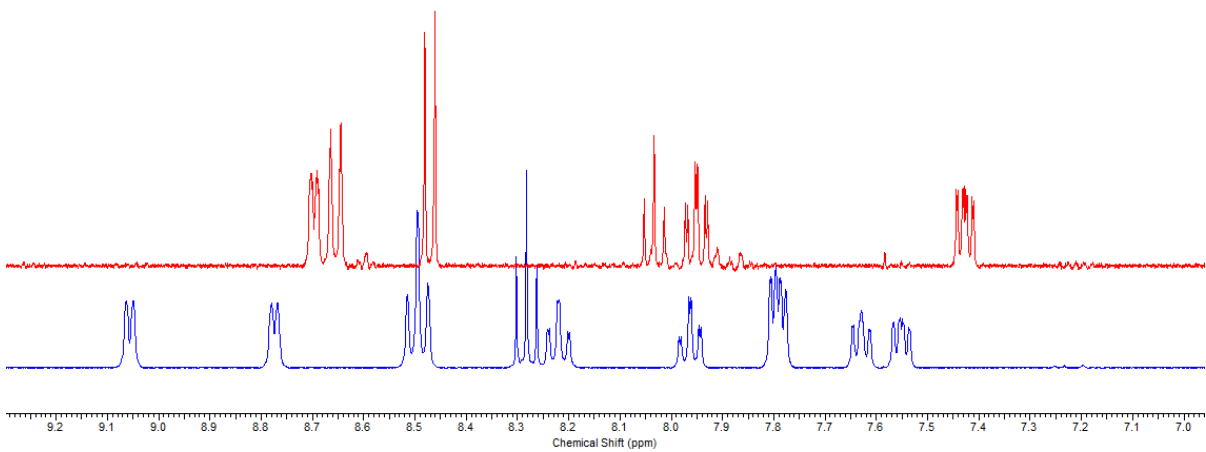


**Figure 2.3** The aromatic region of the  $^1\text{H}$  NMR spectra for compounds **2.1** (blue) and **2.2** (red), showing the simplification of the spectra upon the conversion from bidentate to terdentate.

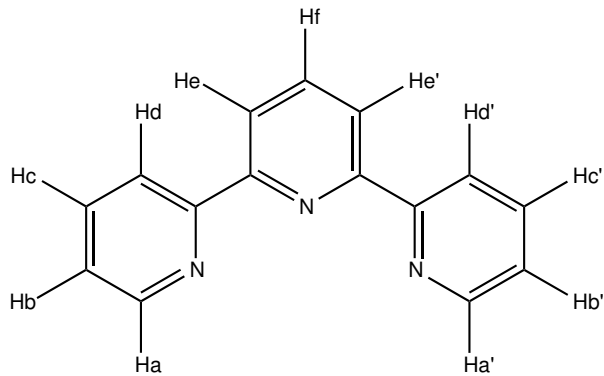


**Figure 2.4** Proton-explicit skeletal drawing of 2,2':6',2''-terpyridine.

the other pendant protons.

As in the case of bidentate compounds, modification of the anion has only minor effects on the NMR spectra. This is the expected behaviour, the conjugated pi system and the lack of protons near the modified anion combine to be susceptible in only a minor fashion.

Carbon NMR ( $^{13}\text{C}$ ) was attempted on the complexes as well. Unfortunately,  $\text{Re}^I$  complexes perform poorly in  $^{13}\text{C}$  NMR experiments, the signal to noise ratio is incredibly

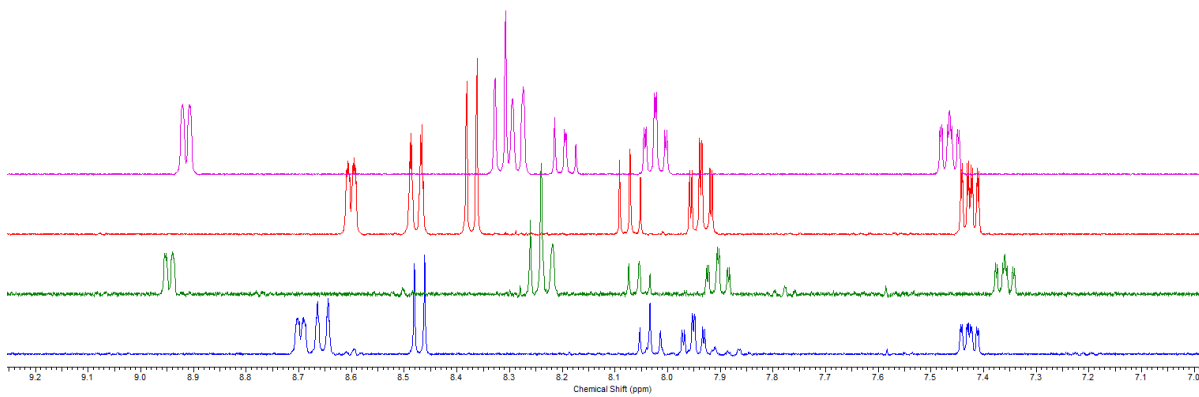


**Figure 2.5** The aromatic region of the <sup>1</sup>H NMR spectra for compounds **2.2** (blue), **2.4** (green), **2.6** (red) and **2.8** (purple).

poor (if a signal is even visible). The effect of this is a lack of <sup>13</sup>C NMR analysis of these compounds in literature, with very few exceptions.<sup>129</sup> Extensive efforts included use of a 500 MHz spectrometer, with 1664 scans to produce the best example, seen in Figure 2.6, with average peak signal to noise ratio (s/n) of only 4 - 5.

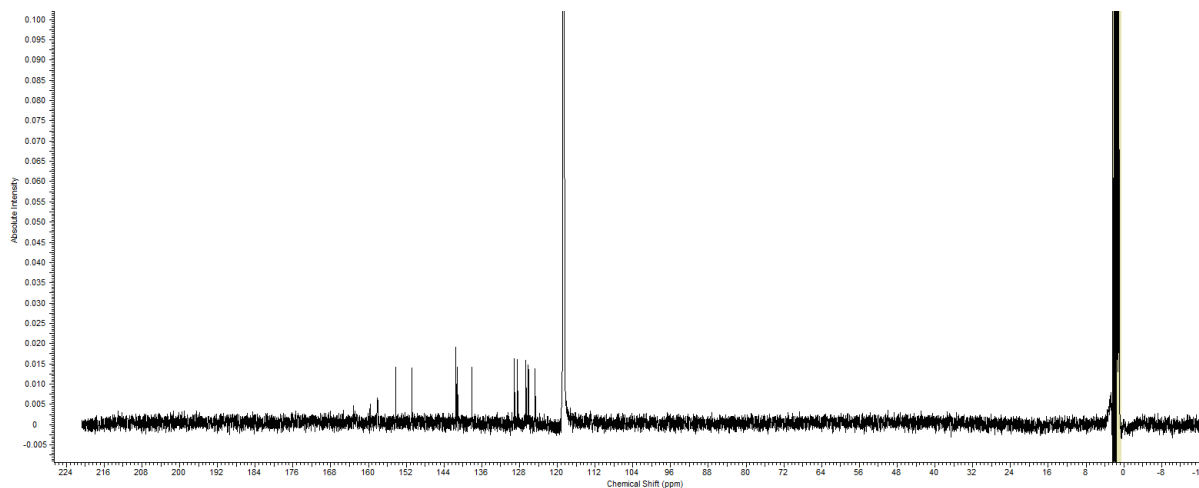


**Figure 2.6** The <sup>13</sup>C NMR spectra of **2.1**. Spectra for other compounds could not be collected.

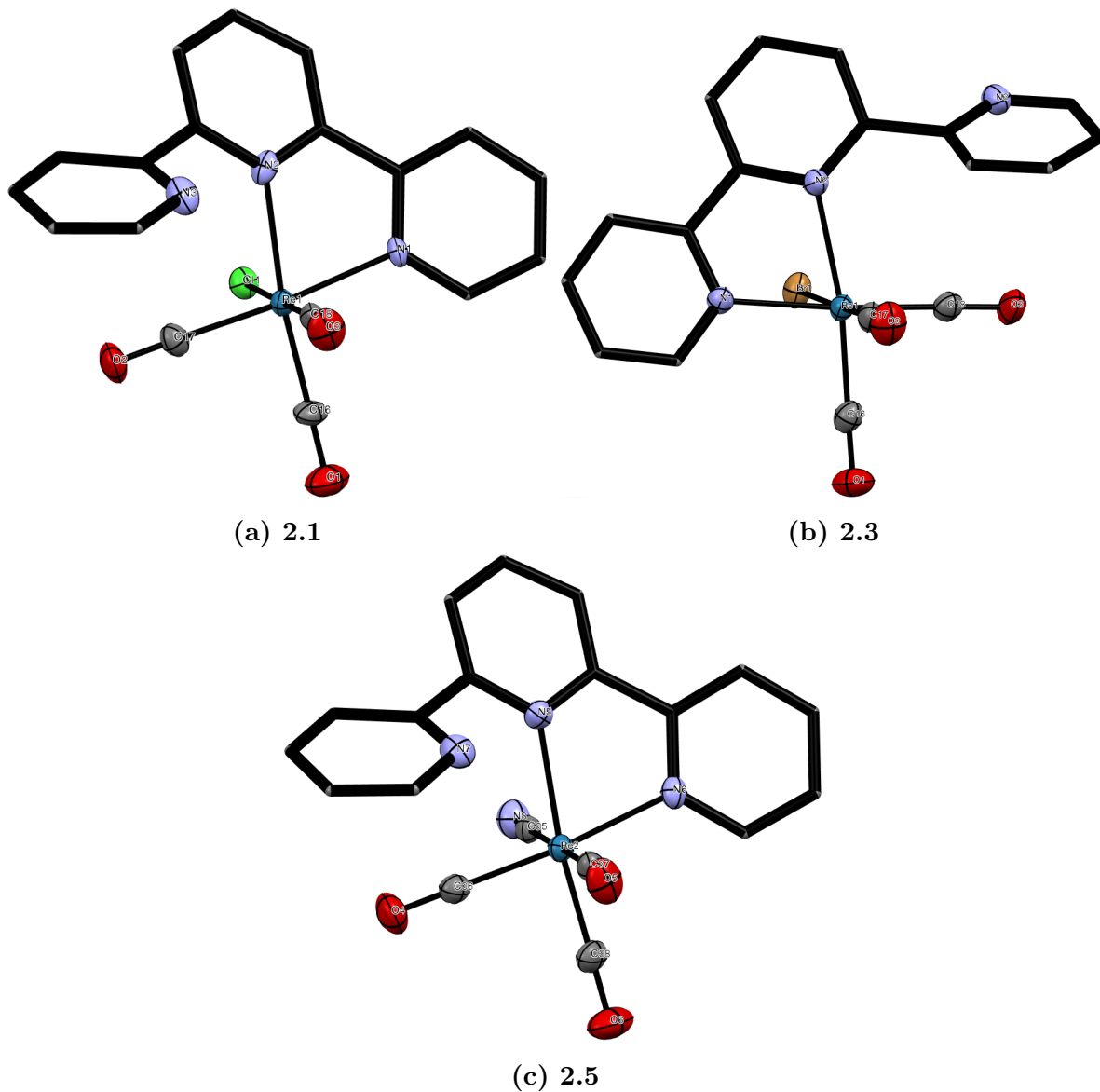


**Figure 2.7** X-ray crystal structure representation for **2.1**, **2.3**, and **2.5**. Co-crystallized chloroform, hydrogen atoms, and thermal ellipsoids of ligand carbon atoms are omitted for clarity.

analyzed. The typical N-Re-N bond angle of  $75^\circ$  is due to the atomic size of rhenium, comparison to the crystal structure of an analogous compound with a manganese atom<sup>142</sup> shows a decrease in the bonding angle for the Re complex by approximately  $4^\circ$  due to an increase of bond length from metal to nitrogen of about  $0.12\text{ \AA}$  for both the central

and terminal pyridines.

The deviation from octahedral is further visible in the rotation of the X-Re-CO plane (X=halide, anion, or other complexed group) by approximately 10 degrees from the right angle relative to the plane of the ligand. The axial halide, anion, or chelated group typically occupies a position slightly departed from the perpendicular, angled to be over the ligand. The reason for the eclipsing is unknown, as no steric interference exists at that site, and analysis of electrostatic or other short-range electronic effects computationally show any interaction between this site and the aromatic rings. In Re<sup>I</sup> complexes, the halide or anion is located axial relative to the plane of the ligand. For the acetonitrile complex with triflate counterion, the acetonitrile occupies the axial position. This site occupation holds through the complete set of x-ray crystal structures with a  $\kappa^2$ -(bipy)Re(CO)<sub>3</sub>X core structure motif deposited in the Cambridge Crystallography Data Centre (CCDC) database,<sup>143</sup> and extends through other  $\alpha$ -diimine complexes seen in our lab and in literature.<sup>73</sup>

**Table 2.2** Solvated and gas phase energy differences between Axial & Trans geometries of  $\kappa^x$ -(terpy)-Re(CO)<sub>5-x</sub>CN (x=2,3)

<u>Bidentate</u>		<u>Terdentate</u>	
E(gas) <sup>a</sup>	E(solution) <sup>b</sup>	E(gas) <sup>a</sup>	E(solution) <sup>b</sup>
14.70	11.87	16.28	16.43

<sup>a</sup> B3LYP SCF energy in kcal/mol.

<sup>b</sup> B3LYP SCF energy in kcal/mol, with PCM solvation in acetonitrile.

The crystal structure for compound **2.5** contains two molecules per unit cell, one of which is solved to have the cyano group in the position trans to the ligand. However, careful analysis of the bond lengths, angles, and torsion data in Table 2.5 shows a remarked similarity between all -CO and -CN groups. Additionally, in an x-ray diffraction pattern, -CN and -CO are difficult to differentiate with certainty. Thus, while the struc-

Structural comparisons between the bidentate samples and the terdentate show many similarities. The loss of one carbonyl always accompanies the chelation of the pendant arm of the ligand. The increased coordination forces the ligand to adopt a more rigidly planar geometry, this is visible in the structure of **2.2** (Figure 2.8a) and **2.8** (Figure 2.8b). Suitable crystals for x-ray analysis were unable to be collected for the remaining complexes.

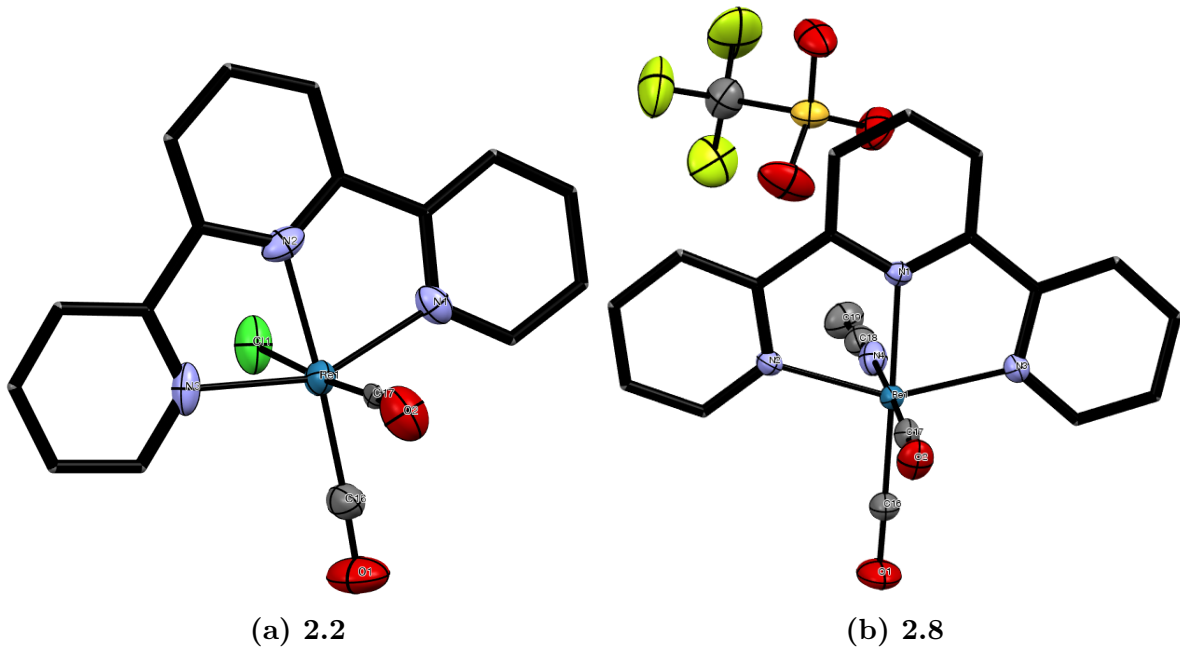


**Figure 2.8** X-ray crystal structure representation for **2.2** and **2.8**. Co-crystallized chloroform, hydrogen atoms, and thermal ellipsoids of ligand carbon atoms are omitted for clarity.

Selected bond lengths, bond angles, and torsions are listed in Table 2.6 and Table 2.7 for products **2.2** and **2.8**. Cell parameters and collection data can be found in Table 2.8.

Both **2.2** and **2.8** structures are pseudo-octahedral in geometry, with *mer* coordinated terpyridine ligand. The carbonyl groups and chloride/acetonitrile form a plane approximately perpendicular to the ligand. As in the  $\kappa^2$ -bidentate samples discussed above, the carbonyls occupy the equatorial and one axial position relative to the ligand,

and the chloride or acetonitrile occupy the remaining axial position. The N-Re-N bond angles remain approximately 75°, and the central pyridyl N to chloride or acetonitrile angle is still approximately 80-85°.

Comparisons between the  $\kappa^2$ -bidentate and  $\kappa^3$ -terdentate samples (**2.1** and **2.2**) highlight the geometrical changes experienced in the thermolysis reaction. The distance from Re to the central pyridyl N has shortened from 2.24 to 2.08 Å. This bond shortening of 0.16 Å signifies increased metal-ligand interaction. This comes at the expense of decreased interaction with the carbonyl groups, with the bond to the planar CO increasing from 1.89 to 1.93 Å and the axial CO bond increasing from 1.901 to 1.975 Å. As the carbonyls experience less  $\pi$  backbonding from the metal, the internal C-O bond shortens by as much as 0.1 Å.

The  $\kappa^3$ -terdentate samples (**2.2** and **2.8**) provide the opportunity to analyse both neutral and cationic species. Due to the weakly coordinated triflate anion in **2.8**, a number of geometric differences arise compared to **2.2**. While the ligand is coordinated by only 0.01 - 0.02 Å closer to the metal atom, the carbonyl groups are 0.04 - 0.1 Å closer, indicating their increased electron donation to the electron poor metal centre. As well, the C-O bonds in the carbonyls are 0.03 - 0.12 Å longer, indicating the increased  $\pi$  backbonding occurring in the cation.

**Table 2.8** Crystal data and structure refinement for compounds **2.2** and **2.8**

Compound	<b>2.2</b>	<b>2.8</b>
Empirical formula	$C_{18}H_{11}N_3O_2ReCl$	$C_{21}H_{14}N_4O_5F_3SRe$
Formula weight (g/mol)	510.95	665.61
Temperature (K)	200	200
Wavelength (Å)	0.71073	0.71073
Crystal System	Triclinic	Triclinic
Space Group	P-1	P-1
a (Å)	8.5275(3)	8.5745(4)
b (Å)	14.2421(5)	11.9805(5)
c (Å)	17.4637(6)	13.0970(5)
$\alpha$ (deg)	77.948(2)	79.748(2)
$\beta$ (deg)	85.684(2)	81.106(2)
$\gamma$ (deg)	79.890	88.091(2)
Volume (Å <sup>3</sup> )	2041.79(12)	1307.99(10)
Z, r (calc) (Mg/m <sup>3</sup> )	4, 2.050	2, 1.993
Absorption coefficient (mm <sup>-1</sup> )	6.494	5.094
Absorption correction	Semi-empirical from equivalents	
Final R indices [ $I \geq 2\sigma(I)$ ]	R1 = 0.0636, wR2 = 0.1018	R1 = 0.0294, wR2 = 0.0673
R indices (all data)	R1 = 0.0985, wR2 = 0.1110	R1 = 0.0366, wR2 = 0.0700

### 2.3.3 Infra-Red Spectroscopy

Conversion of bidentate to terdentate species was confirmed utilizing Fourier Transform Infrared (FTIR) spectroscopy. A small sample of powder product was placed on the Agilent Cary 630 FTIR spectrometer, with a  $2 \text{ cm}^{-1}$  resolution. The instrument is fitted with a diamond ATR for solid sample analysis. Spectra are the Fourier transform of 16 scans for each sample.

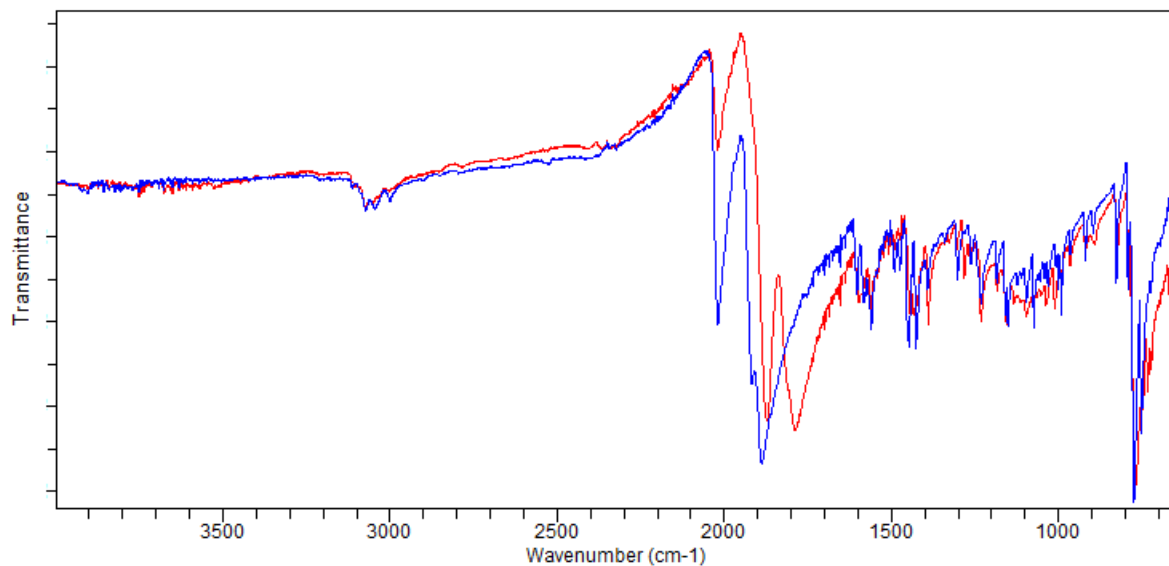


**Figure 2.9** FTIR Spectra for complexes **2.1** (blue) and **2.2** (red).

Analysis of the results in Figure 2.9 shows the significant reduction of one peak in the ca.  $2100 \text{ cm}^{-1}$  region. This peak is in the CO stretching frequency, the frequency of the peak lost in thermolysis is indicative of a weakly coordinated carbonyl group. A splitting occurs for the other large peak and its shoulder in the conversion from bidentate to terdentate, from  $1890$  to  $1790 \text{ cm}^{-1}$ , indicating the further weakening of the metal carbonyl bonds remaining in the complex. This weakened bond is likely the carbonyl co-planar to the ligand, analysis of the x-ray crystal structure shows the CO bond to be  $0.1 \text{ \AA}$  longer than that of the axial carbonyl. This identification is supported by the

DFT methods discussed below.

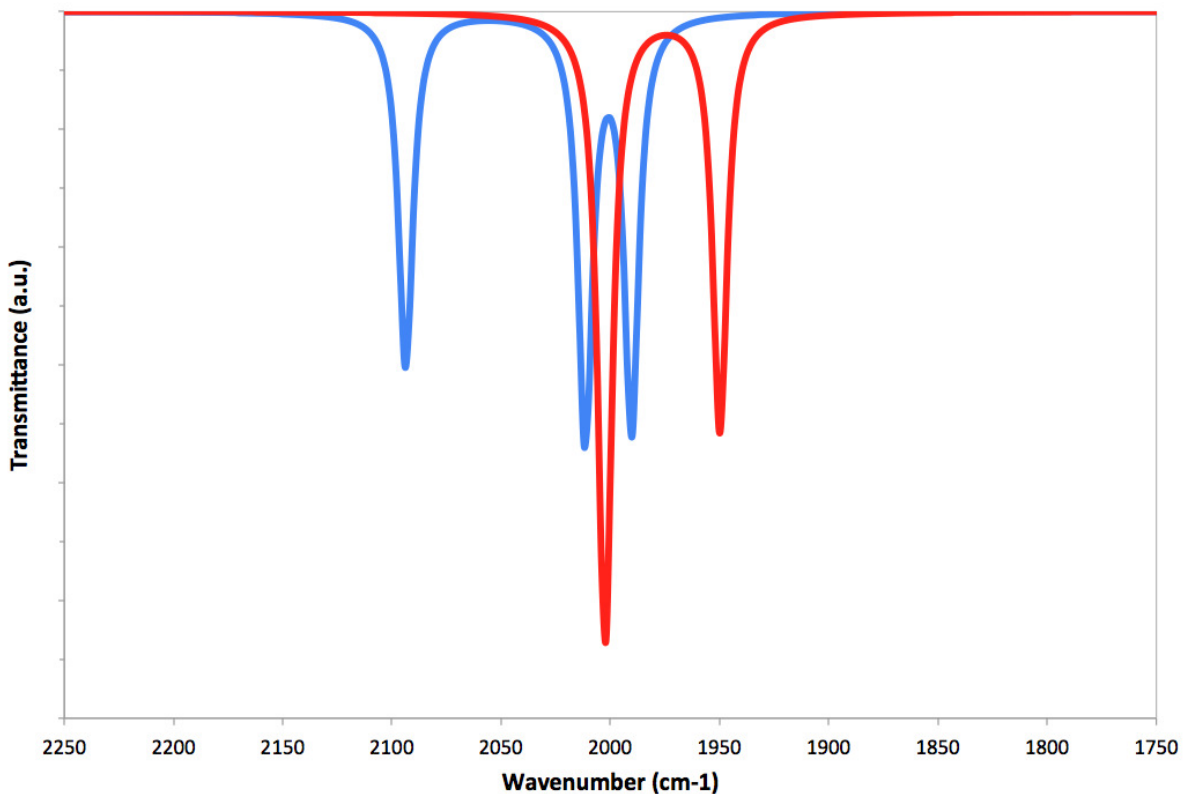


**Figure 2.10** DFT predicted FTIR spectra for **2.1** (blue) and **2.2** (red).

FTIR spectra were predicted using molecular frequency calculations of DFT optimized structures. Prediction of this spectra was performed as a verification of the optimized structures discussed in subsection 2.3.2 above. The calculation identifies stretching or bending harmonic energies in optimized structures. The computed spectra in Figure 2.10 shows three peaks for **2.1**, at 2094, 2012, and 1990  $\text{cm}^{-1}$ . The relative location of these peaks corresponds to those seen in Figure 2.10 for **2.1**, but are shifted by approximately 100  $\text{cm}^{-1}$  to higher energy relative to the experimental. This is characteristic of DFT calculations, which usually over-report frequencies by approximately 0.96 for B3LYP calculations.<sup>144</sup> Similarly, for **2.2**, peaks are seen at 2000 and 1950  $\text{cm}^{-1}$ , compared to the 1890 and 1790  $\text{cm}^{-1}$  peaks seen experimentally. This computed value

reflects the shift to lower energy carbonyl stretching from **2.1** to **2.2**, and echoes the experimental spectra well.

Further analysis of other spectra were not successful in identification of any additional molecular properties, with the exception of a series of strong peaks appearing in the 1200–1300  $\text{cm}^{-1}$  range for samples **2.7** and **2.8**, confirming the presence of the triflate anion from the  $-\text{SO}_3^-$  group vibrations (Figure 2.11). Additionally, the small peak present at 2270  $\text{cm}^{-1}$  in the terdentate sample corresponds to the weakly coordinated acetonitrile occupying the molecule's axial position.

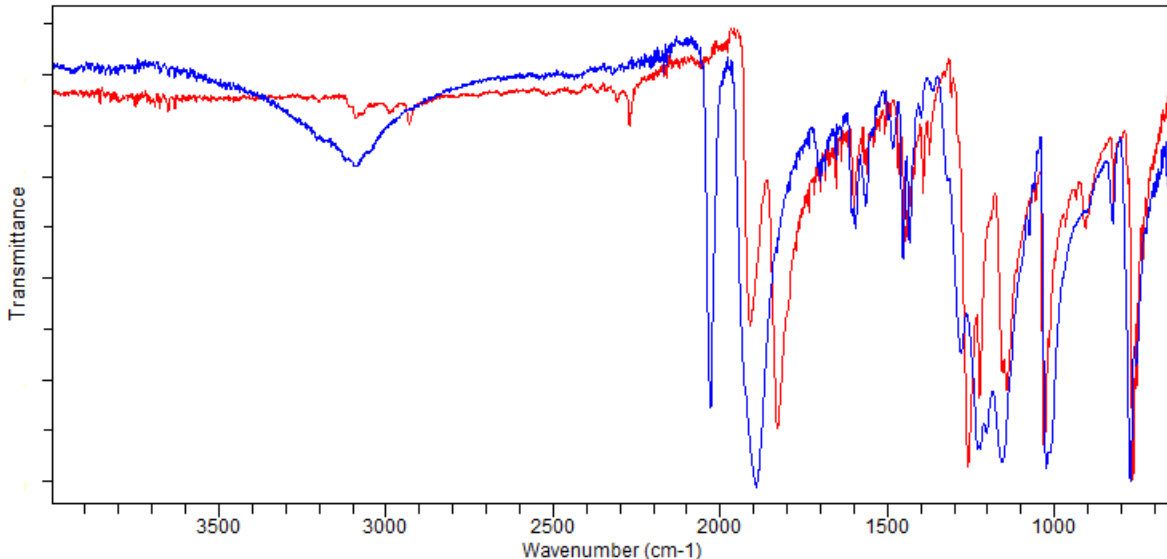


**Figure 2.11** FTIR Spectra for complexes **2.7** (blue) and **2.8** (red).

### 2.3.4 Photophysical Properties

A striking observation upon the conversion of the bidentate species into the terdentate complexes is that these new compounds have a substantially darker colour that reflects a significant change in the photophysical properties. This effect was investigated using a combination of UV-visible spectroscopy and DFT modelling. Spectra were collected on a Agilent Cary 5000 UV-Vis-NIR Spectrophotometer. The stronger absorbance of

the terdentate complexes compared to the bidentate precursors is evident in the UV-Vis spectra of these species, and is presented in Figure 2.12 and Figure 2.13. These spectra were obtained in Dimethylsulfoxide (DMSO) with approximate concentrations of 0.01 mM for bidentate, and an order of magnitude lower (0.001 mM) for the terdentate analogues. The terdentate complexes have more intense absorbance for higher energy ligand UV-based  $\pi-\pi^*$  transitions (<400 nm) and certainly a richer visible absorption profile that involve the  $d-\pi^*$  transitions. These features are responsible for the colour change observed.

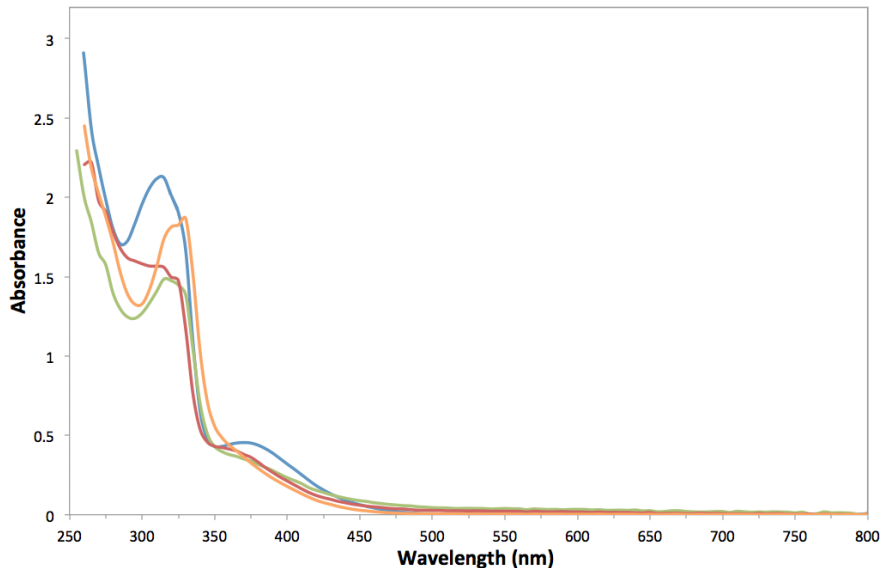


**Figure 2.12** UV-Vis spectra for compounds **2.1** (blue), **2.3** (green), **2.5** (red), and **2.7** (orange) at 0.01 mM concentration.

The UV-Vis spectra were modelled using TD-DFT computations within Gaussian 09, using the B3LYP functional with the LanL2DZ basis set and effective core potentials for the rhenium atom, and the TZVP basis set for all lighter atoms. Solvent was simulated using the integral equation formalized variant of the PCM solvation model, with DMSO as the solvent.

The resulting computed spectra were excellent matches to the experimental spectra.

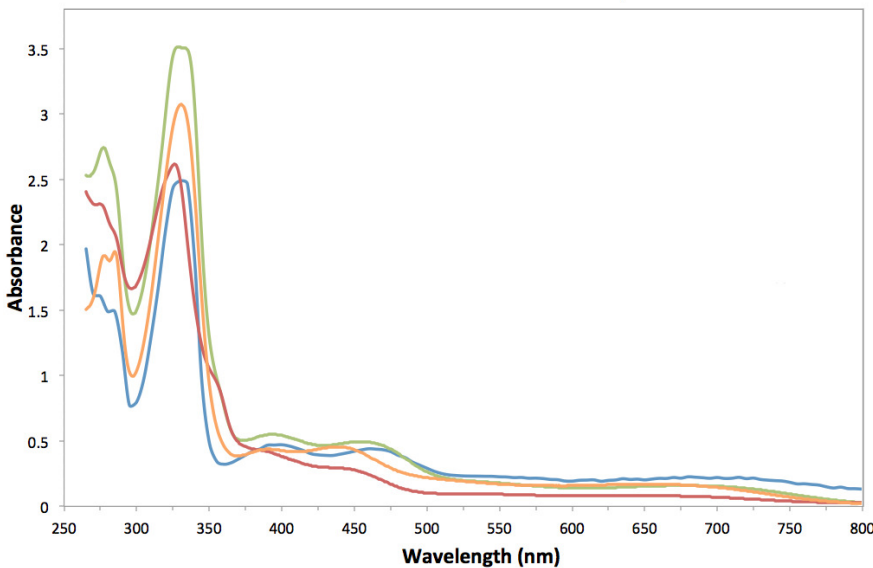


**Figure 2.13** UV-Vis spectra for compounds **2.2** (blue), **2.4** (green), **2.6** (red), and **2.8** (orange) at 0.001 mM concentration.

The similarity of the spectra between the bidentate species and as well as the terdentate species indicates that parallel electronic transitions appear within these two groups. Specifics will be discussed for the chloro compounds, **2.1** and **2.2**, but strong parallels exist for all species. Plots of experimental and computational data for these two complexes are presented in Figure 2.14 and Figure 2.15, respectively.

Common to all bidentate compounds were peaks at wavelengths of 315-320 nm, and peak shoulders near 350-375 nm (Figure 2.12). In the case of **2.1**, the computational results suggest that the experimental band centred at  $\lambda = 315\text{-}320\text{ nm}$  ( $31750\text{-}31250\text{ cm}^{-1}$ ) primarily arises from two electronic transitions. The first is from HOMO-3 to LUMO, a  $\pi\text{-}\pi^*$  transition, while the second major contribution is the excitation from HOMO to LUMO+2, which is a  $d\text{-}\pi^*$  transition. The TD-DFT calculations suggest that the experimental band centred at  $\lambda = 370\text{ nm}$  ( $27030\text{ cm}^{-1}$ ) corresponds to a calculated transition at approximately 400 nm, that is a  $d\text{-}\pi^*$  (HOMO-1 to LUMO) absorbance. Computed plots of molecular orbitals are included in Appendix C, Molecular Orbitals

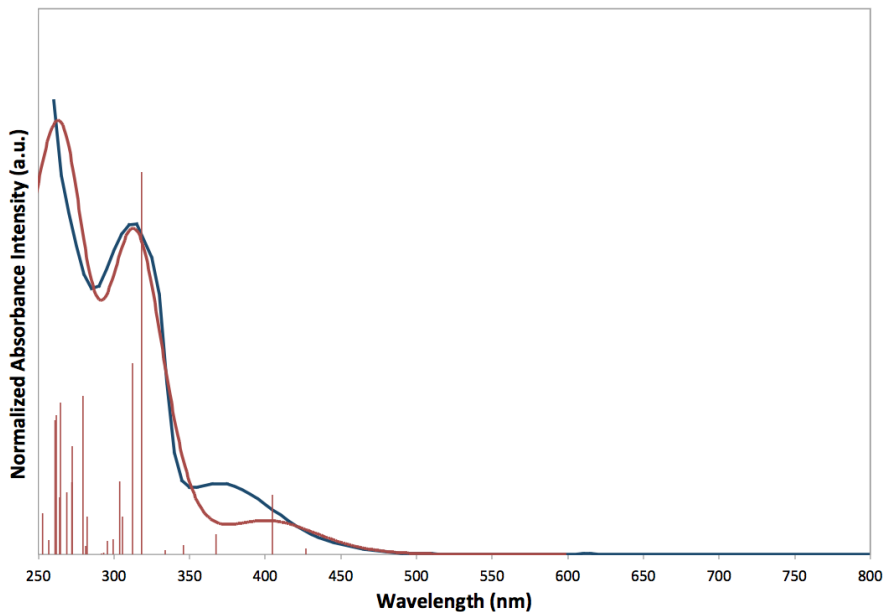


**Figure 2.14** Plots of the experimental and computed UV-Vis spectra for compound **2.1**. The blue curve shows experimental result. The red vertical lines show the calculated transitions and relative intensities from the TD-DFT calculations, while the red curve shows the gaussian convolution with peak width at half height of 0.250 eV.

Diagrams, Figures C.1 to C.8.

Like the bidentate samples, the spectra for the terdentate samples are quite similar to one another. In general, all of these species have much higher absorbance coefficients than their bidentate analogues; all contain long trailing absorptions across the wavelengths analysed. For terdentate complex **2.2**, the four experimentally observed UV-Vis absorptions observed are made up of six computed transitions. The computational model provided two equal and strong transitions appearing at 308 and 325 nm to generate the experimental band centred at  $\lambda = 330 \text{ nm}$  ( $30300 \text{ cm}^{-1}$ ). These arise from a transition from HOMO-5 to LUMO, a Cl lone-pair to terpy  $\pi^*$  orbital absorption, and from HOMO-3 to LUMO, which is a ligand centred  $\pi-\pi^*$  transition. All of the lower energy transitions are dominated by MLCT bands. The experimental band centered at  $\lambda = 400 \text{ nm}$  ( $25000 \text{ cm}^{-1}$ ) arises from an electronic transition from HOMO to LUMO+3

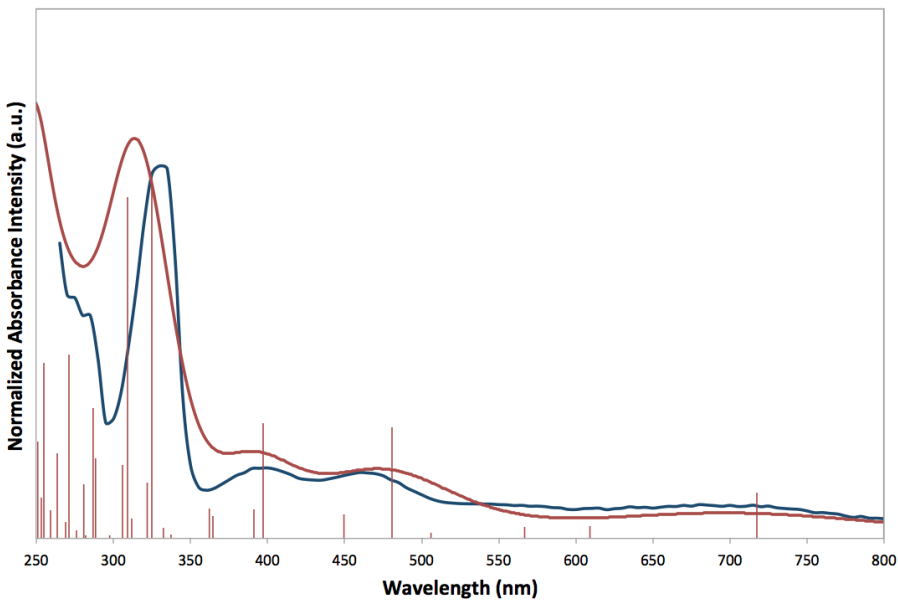


**Figure 2.15** Plots of the experimental and computed UV-Vis spectra for compound **2.2**. The blue curve shows experimental result. The red vertical lines show the calculated transitions and relative intensities from the TD-DFT calculations, while the red curve shows the gaussian convolution with peak width at half height of 0.250 eV.

which is  $d-\pi^*$  in nature. The absorbance centred at  $\lambda = 460$  nm ( $21740\text{ cm}^{-1}$ ) corresponds to two MLCT  $d-\pi^*$  transitions; HOMO-2 to LUMO and HOMO-1 to LUMO+1. Finally, the broad experimental band 680-715 nm ( $14700\text{-}14000\text{ cm}^{-1}$ ) arises from the electronic transition appearing at 718 nm, which is the excitation of a  $d$ -electron in the Re-centered HOMO to the ligand  $\pi^*$  LUMO.

### 2.3.5 Fluorescence

Fluorescence data was collected for **2.1** and **2.2** using an Agilent Cary Eclipse Fluorescence Spectrophotometer, using a 5 nm excitation slit and emission slit, using excitation wavelengths selected to correspond to the centre of UV-Vis absorption bands. Data was collected for spectra in N,N-dimethylformamide (DMF) to simulate the photocatalytic reaction environment (see chapter 3). Spectra are shown in Figure 2.16 for **2.1** and

**2.2** with their UV-Vis absorption spectra for comparison. Data is normalized to equal concentration for each sample in fluorescence and absorbance.

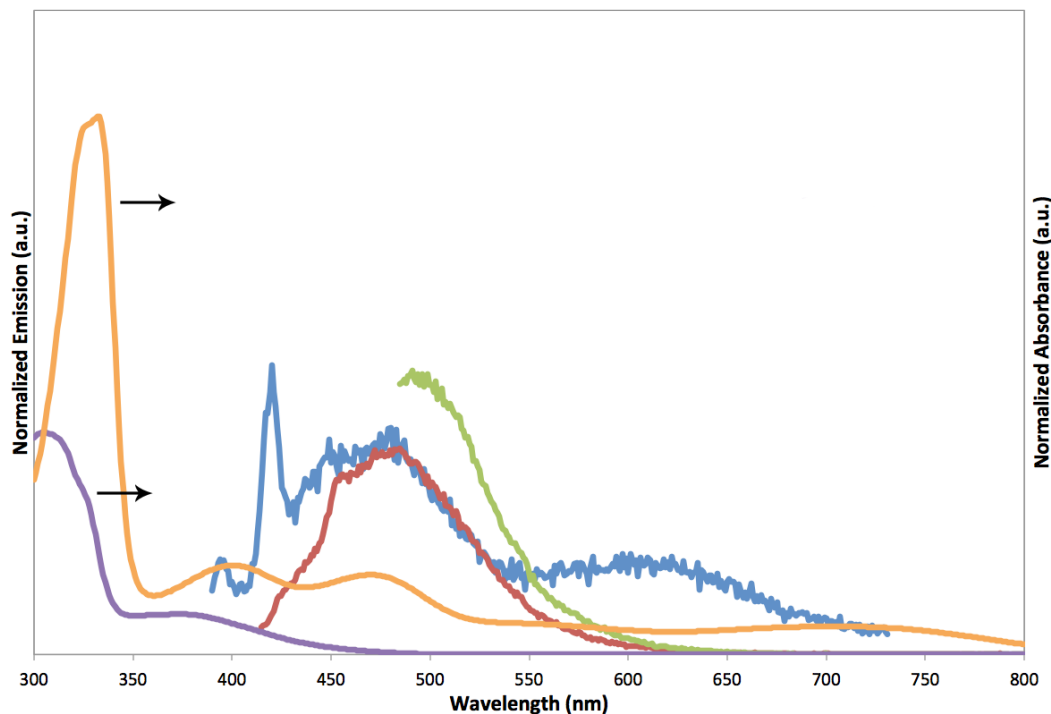


**Figure 2.16** UV-Vis and fluorescence spectra for **2.1** and **2.2**. Fluorescence of **2.1** from excitation of 373 nm (blue), excitation of **2.2** by 400 nm (red) and 470 nm (green) are shown, along with the absorption spectra of **2.1** (purple) and **2.2** (orange).

Clearly the transformation from bidentate terpyridine to terdentate ligand has significant effect on the interactions of these Re compounds with visible light. While the terdentate sample is excited at various wavelengths (that should correspond to different absorption bands), the emission appears to be from one single band centred at ca. 485 nm. An emission band appears similarly in bidentate, centred at 480 nm, with a second, broad, weaker band appearing centred around 600 nm. The sharp peak observed at 420 nm is present in the DMF solvent blank as well.

Interestingly, emission is not seen with the naked eye with 400 nm excitation for the terdentate, while emission from the bidentate emission is a very strong, white light.

This may be due to self-absorbance in the terdentate samples, emission of 490 nm is easily absorbed by the molecule. In the bidentate, no absorbance bands correspond with emission bands shown, these appear to the naked eye as a white emission.

## 2.4 Conclusions

This work reported the first crystallographically authenticated rhenium(I) terpyridine terdentate complexes and thus expanded upon the prior limitations of Re coordination complexes. These terpyridine complexes are accessed via a simple, highly efficient, solid-state thermolysis pathway. They expand upon the known  $\alpha$ -diimine photophysical properties, with enhanced metal to ligand,  $d-\pi^*$  electronic transitions, occurring more frequently and with lower energy than in the associated bidentate compounds. These observations are supported by computational TD-DFT results, affording an expanded understanding of the transition bands. Modification of the bidentate and terdentate species has been shown, the synthetic success of a triflate moiety should facilitate further development of reactivity and provides an opportunity for synthetic and catalytic studies.

analysis methods, solvent, sacrificial reductant, pH, presence of electrolyte, presence of H<sub>2</sub>O, or variation of anion (X=Cl, Br, OTf, CN) shows no change of this inactivity. Testing of  $\kappa^2$ (bipy)Re(CO)<sub>3</sub>Cl under the same reaction and testing conditions shows production of approximately 6 mL CO from CO<sub>2</sub> ( 20% conversion) in 1 hour of photolysis with visible ( $\lambda > 400$  nm) light, verifying the method and isolating the particular catalysts as the ineffective species.

### 3.2.3 Rationalization of Results

The lack of reactivity of the  $\kappa^2$ (terpy)Re(CO)<sub>3</sub>X motif of complexes contrasting to the activity of the originally published  $\kappa^2$ (bipy)Re(CO)<sub>3</sub>X indicates significant influence of the ligand on the reaction. Kurz *et al.* demonstrated the requirement for fluorescence for successful catalytic candidates.<sup>132</sup> The explanation for this is the requirement for a stable, long-lasting excited state, with lifetime greater than that of the timescale of the electron abstraction from the sacrificial amine. Observed fluorescence demonstrates the lack of non-radiative relaxation pathways, considered to be an analogue for the extended lifetime of the excited state. Sample **2.2** shows only poor fluorescence (see chapter 2, subsection 2.3.5). While the complex is able to absorb light across the spectrum, and has HOMO to LUMO transitions with high enough energy<sup>i</sup> for the catalyzed reduction of CO<sub>2</sub> to CO, it appears as if the catalysis is not initiated due to a short excited state lifetime.

Explanation for the lack of CO production observed in the attempted photochemical reduction of CO<sub>2</sub> by bidentate sample **2.1** and others must come from some other area. These samples are quite fluorescent, emission from the powder sample can be seen with the naked eye with simulation by a 405 nm laser pen under ambient light environments.

---

<sup>i</sup>Electrochemical reduction of CO<sub>2</sub> in similar environments takes 1.7-2.1 V, equivalent to HOMO-LUMO transitions from 590-750 nm.<sup>152</sup>

Other substituted bipyridine ligands are known to be active for photocatalytic reduction,<sup>67,132</sup> thereby suggesting the most likely conflicting feature of the terpyridine ligand to be the pendant arm itself.



**Figure 3.1** A photograph of fresh (left) and aged (right) catalyst mixtures, showing the change from yellow to red in five days.

Importantly, two clues come from the reaction mixture: under intense visible light in the presence of CO<sub>2</sub> the compound bleaches from bright yellow (see the left vial, Figure 3.1) to a very faint yellow-green. Colour does not return after storage in the dark, bubbling of new CO<sub>2</sub>, or other manipulations. Secondly, a mixture of sacrificial amine, DMF, and catalyst **2.1** in ratios identical to what is required in the reaction mixture changes colour from a yellow to a deep red irreversibly after approximately five days at ambient conditions, as shown in Figure 3.1.

The most likely cause for the bleaching of the solution is the disassociation of terpyridine ligand from the metal centre. The colours seen in the catalyst are all due to metal-ligand interaction, and the UV-Vis spectrum of free terpyridine in solution is located solely in the UV range ( $\lambda^{\max} \approx 285$  nm).<sup>153</sup> The labilization can be a photoinduced process.<sup>154</sup>

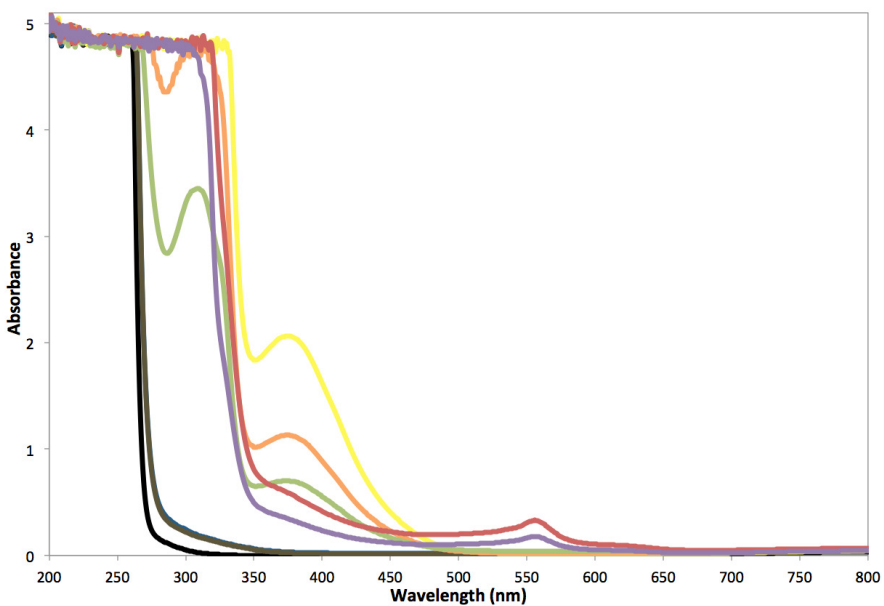
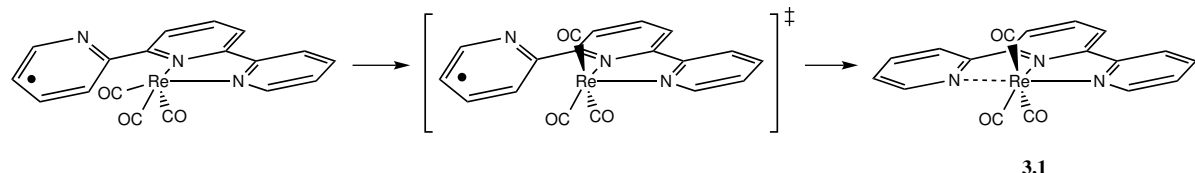


**Figure 3.2** UV-Visible spectra of freshly prepared and aged catalyst mixture. DMF, DMF-TEOA (5:1), and DMF-TEOA +  $Et_4NCl$  (1 mM) are shown in black, blue and olive, respectively. Fresh catalyst is shown in yellow (1 mM catalyst), orange (0.5 mM) and green (0.25 mM). Aged catalyst is shown in red (1 mM) and purple (0.5 mM).

The UV-visible spectra was obtained for the red compound formed after 5 days of ageing, showing some distinctive modifications (see Figure 3.2). A peak appears at ca. 560 nm, and the metal to ligand  $d-\pi^*$  peak at 470 nm is reduced. Additionally, the fresh catalyst has a valley in the spectrum at ca. 285 nm, while the aged sample does not and in fact has increased adsorption at energies above 310 nm.

Other complexes may be formed that deactivate the catalyst, including the forma-



**Scheme 3.1** Formation of **3.1** from catalytic excimer via reorganization of carbonyls and chelation of the pendant arm.

tion of a cationic tridentate tricarbonyl complex, seen in Scheme 3.1. This species can be formed by the rearrangement of the carbonyl ligands from the *fac* orientation to a *mer*, migration of one carbonyl to the open site axial to the ligand achieves this reorganization. Once the *mer* species is formed, the open site on the metal centre is oriented towards the pendant arm of the terpyridine ligand, coordination of that group to the metal centre results in compound **3.1**. The UV-Visible spectra of this species is not isolated, however, DFT predicted UV-Vis is shown in Figure 3.3, and compared to the experimental red product, these spectra do not correlate. This reorganization may still occur in the reactant solution, but it does not appear to be the primary deactivation pathway.

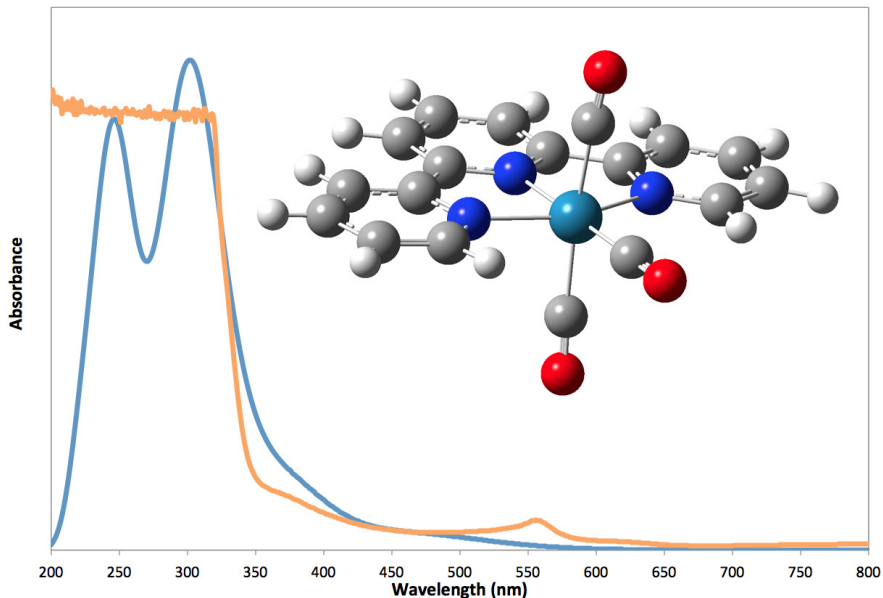


**Figure 3.3** Computational structure (inset) and predicted UV-Vis absorption spectra of  $[\kappa^3\text{--(terpy)}\text{--Re}(\text{CO})_3]^+$  and experimental spectra of the aged catalytic mixture (orange).

Another deactivation product may be the formation of triethanolamine-catalyst adducts.<sup>129</sup> In the presence of DMF, TEOA has been shown to bind to the open site of the excimer via the amine's oxygen atom. This is susceptible to insertion of CO<sub>2</sub> to form a –OC(O)C–

$\text{CH}_2\text{CH}_2\text{N}(\text{CH}_2\text{CH}_2\text{OH})_2$  group. DFT studies on these two compounds suggest that they may be a coloured species, with predicted UV-Vis showing lower energy absorption than the catalyst itself (a red shift), demonstrated in Figure 3.4. The experimental red mixture UV-Vis spectra is overlaid, showing lack of correlation to the Ishitani compounds.

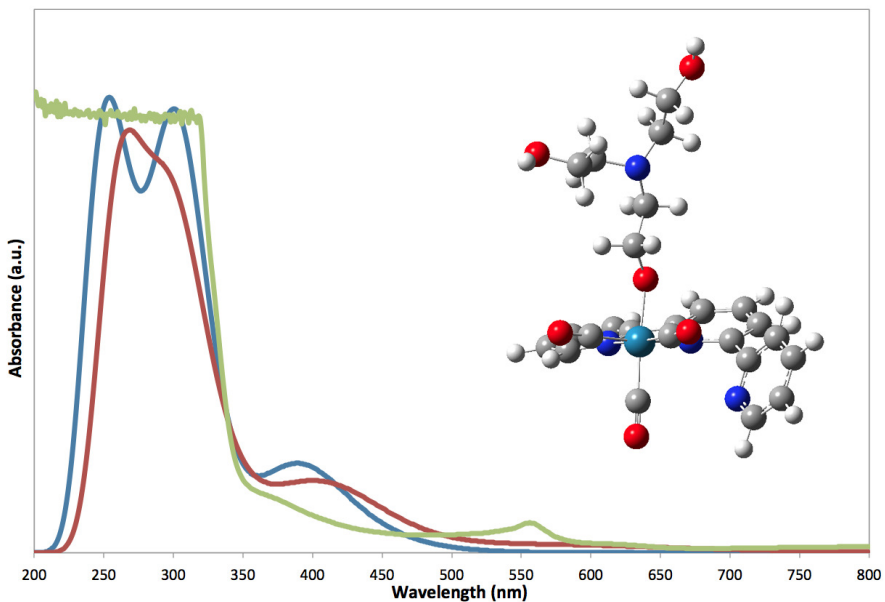


**Figure 3.4** Computational structure (inset) and DFT predicted UV-Vis absorption spectra for **2.1** (blue), the TEOA complex proposed by IshitaniFigure 3.4 (red), and experimental spectra of the aged catalytic mixture (green).

Neither the tricarbonyl terdentate nor the Ishitani complexes correlate to the observed spectra in Figure 3.2. Identification of a compound solely by its spectra is not possible, however, some characteristics could be predicted. It is likely that there is a significant modification of the environment around the metal centre, previous observed electronic transitions that occur at that energy are due to metal  $d$  to ligand  $\pi^*$  interactions. Ligand  $\pi$  to  $\pi^*$  transitions appear at much higher energy, and modification of those interactions could explain the lack of valleys observed in the UV region (at 285 nm). Further determination of the complex is not possible with the collected data.

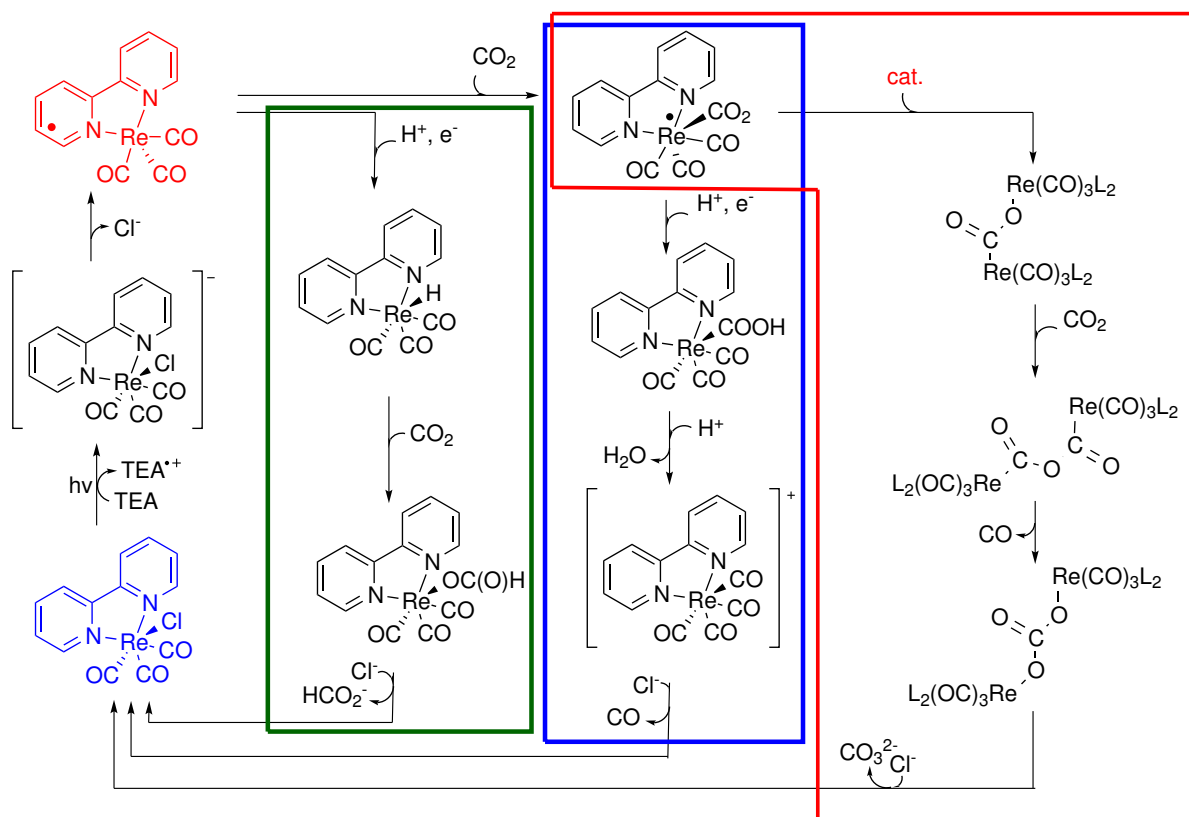
Attempts to isolate this red compound were unsuccessful. It appears to be highly soluble in the reaction mixture, not allowing for isolation via solvent extraction. DMF and TEOA are high-boiling point solvents, any attempts to remove solvent via distillation (even at low pressure) required temperatures approaching the thermolysis temperature for synthesis of the terdentate compounds. Further investigation is required to isolate the product.

### 3.3 Conclusions

Experimental data shows the inactivity of these catalysts for photoreduction of CO<sub>2</sub> under a range of experimental conditions. These same conditions show conversion using  $\kappa^2(\text{bipy})\text{Re}(\text{CO})_3\text{Cl}$  as the photoreductant, signifying the validity of experimental setup. The inactivity may be due to formation of inactive side-products or ligand labilization (for the case of bidentate catalyst) or due to the short excited state lifetime of the terdentate catalyst.

Catalyst mixtures appear to form a new compound after ageing. Although isolation was not achieved, this red product was investigated via UV-Vis spectroscopy, the spectra was compared to DFT calculated spectra for two potential deactivation products. The spectra do not align, suggesting that the red product is some as of yet unknown compound.

addition and the release of a molecule of  $\text{H}_2\text{O}$ . This is essentially the Reverse Water-Gas Shift Reaction (RWGSR), wherein protons are made available from decomposition of the sacrificial amine instead of from the decomposition of  $\text{H}_2$ .<sup>162</sup> These three mechanistic pathways will be referred to as the ‘bicarbonate’ mechanism, the ‘formate’ mechanism, and the ‘water-gas shift’ mechanism, respectively.

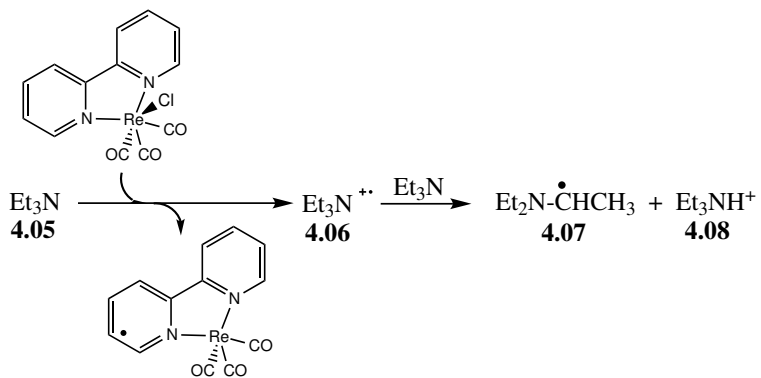


**Scheme 4.1** An overview of the mechanistic pathways of photochemical  $\text{CO}_2$  reduction. Catalyst is shown in blue, and the excimer species in red. The bicarbonate mechanism is boxed in red, the formate mechanism in green, and the water-gas shift mechanism in blue.

Each of the mechanistic pathways identified in Scheme 4.1 was studied, using DFT methods. Structures (using 2,2'-bipyridine as the bidentate ligand, and triethylamine as the sacrificial reductant) were optimized to ground or transition states using TurboMole

6.5 software,<sup>163,164</sup> with the TPSS meta-GGA XC functional.<sup>165</sup> This functional shows good results with organometallic complexes, while maintaining reasonable calculation times. The B3LYP functional is noted for its underestimating of transition state barriers, a complaint not levelled against TPSS.<sup>139</sup> The def2-TZVP all electron basis set was used for all atoms.<sup>137,166</sup> The TurboMole program utilizes a number of algorithms and techniques to significantly speed up the calculation times, without compromising accuracy.<sup>167–175</sup> Grimme's dispersion correction (version 3) was included in the calculations.<sup>176</sup> Intermediates and transition states were verified by frequency analysis,<sup>172,177,178</sup> with further verification of transition states by performing dynamic reaction coordinate calculations to determine the Intrinsic Reaction Coordinates (IRCs). The effects of solvation were calculated using the Conductor-like Screening Model (COSMO) implemented in TurboMole,<sup>179</sup> which is a continuum solvation model implicitly surrounding the solute molecule. Code was developed to assist with automating and managing the computational jobs (see chapter 5).

Many of the intermediates have been synthesized in various studies,<sup>157,180–182</sup> indicating their reasonable stability. While individual portions of the mechanisms have been studied computationally in the past,<sup>148–150</sup> no overarching study has compared methods relative to each other. Furthermore, while the formation of CO with H<sub>2</sub>O is the most anticipated pathway (due to the lack of formation of bicarbonate or formate in most studies), no literature pathway exists to explain the addition of CO<sub>2</sub> to the open site of the radical catalytic species without a tri-molecular reaction step (catalyst, CO<sub>2</sub> and H<sup>+</sup> together) or without formate reorganization. Furthermore, no mechanism proposed thus far explains the <sup>12</sup>CO to <sup>13</sup>CO isotopic exchange demonstrated by Lehn's group in 1986.<sup>67</sup> These reaction features are ignored by the studies, which prefer to focus only on the reduction of CO<sub>2</sub>, starting from the catalyst-CO<sub>2</sub> adducts and ending with release

**Scheme 4.3** Decomposition pathway for the sacrificial amine.

by the incident photons; this process is a photocatalyzed activation. The reaction typically requires incident light of 400 nm,<sup>66</sup> this high energy input allows for the excitation pathway to be followed. The potential energy diagram for these steps are shown in Figure 4.1.

**Table 4.1** Energies for the reaction steps in the photoinduced excimer formation pathway

Steps	Energy(gas) <sup>a</sup>	Energy(dmf) <sup>b</sup>
<b>4.01</b> → $\text{3MLCT}$	42.81	53.40
<b>4.01</b> <sup>3MLCT</sup> + <b>4.05</b> → <b>4.02</b> + <b>4.06</b>	81.45	-5.80
<b>4.02</b> → <b>4.03</b> + <b>4.04</b>	50.82	15.44
<b>4.06</b> + <b>4.05</b> → <b>4.07</b> + <b>4.08</b>	-1.08	-2.92

<sup>a</sup> TPSS energy in kcal/mol.

<sup>b</sup> TPSS energy in kcal/mol with COSMO solvation in DMF.

Some small geometry changes occur signifying the change in electron structure in the formation of the excimer species. One metric analyzed in polyaromatic non-innocent ligand redox reactions is the bonding distance between aromatic rings.<sup>184</sup> From ground state to triplet MLCT complex the C-C<sub>(bpy)</sub> distance decreases from 1.47 Å to 1.42 Å. This 0.05 Å decrease is noted in many previous experiments and calculations for anion radicals.<sup>184–188</sup> Other key bond lengths and angles include the ligand to metal N-Re bonds

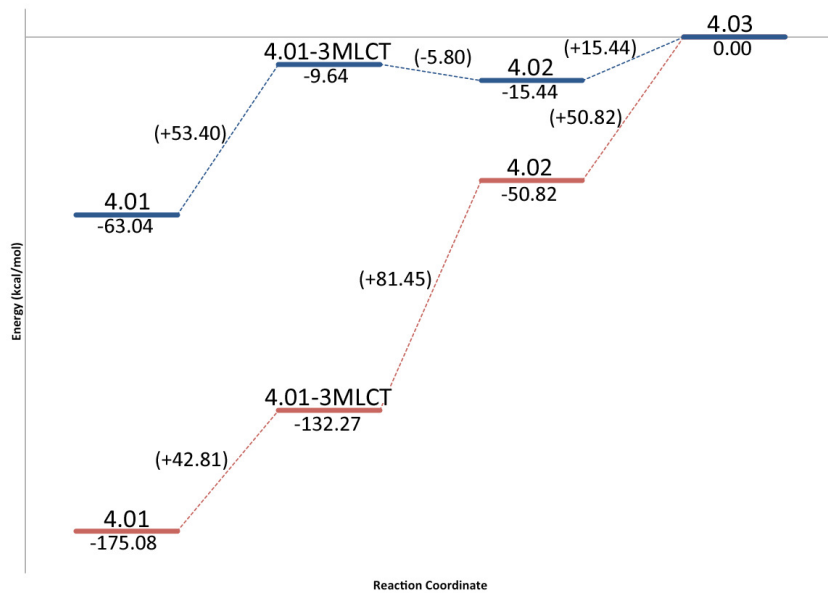


**Figure 4.1** Potential Energy Surface for the production of the excimer. Gas phase energies in red, DMF solvated energies in blue. A larger version can be seen in Appendix D, Figure D.2.

and carbonyl to metal C-Re bonds, the addition and subtraction of electrons to and from the complex impact the bond lengths. As the reaction proceeds, for example, the calculated Re-N distance in solvated structures decreases from 2.19 Å in the ground state catalyst to 2.14 Å in the neutral radical excimer. Similarly, the distance from the metal to the axial carbonyl decreases from 1.92 to 1.89 Å in the same circumstances. Bond length changes of 0.05 Å demonstrate a change has occurred in the electron configuration around the metal centre.

#### 4.2.2 The ‘Bicarbonate’ Pathway

The bicarbonate pathway is shown in the red box in Scheme 4.1, with details shown in Scheme 4.4, starting from the excimer species. This pathway has been studied in the literature, but many details of the mechanism have not yet been explored. Previous com-

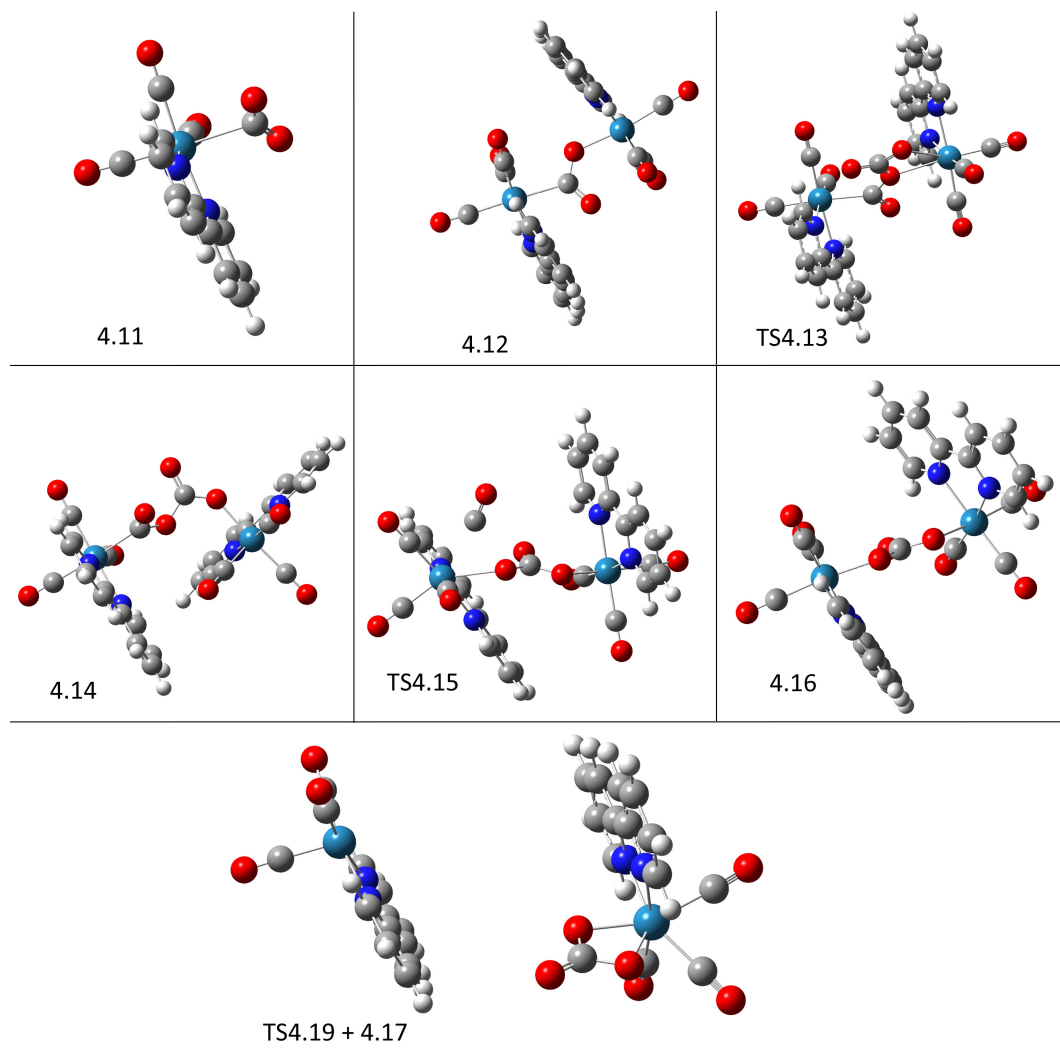


**Figure 4.2** DFT calculated structures for the ‘bicarbonate’ mechanistic pathway. Atoms are coloured as follows: carbon - grey, nitrogen - blue, oxygen - red, hydrogen - white, rhenium - teal.

of *ca.* 1.9 Å, this is a very weak bond. The formation of this complex requires only 6.37 kcal/mol, the electron is unpaired in this new structure as well. An additional electron is required to form a more stable compound. This unstable complex is able to extract a hydrogen from triethylammonium ( $\text{Et}_3\text{NH}^+$ , **4.08**) to continue with the ‘water-gas’ pathway (see below subsection 4.2.4), or combine with a second molecule of the

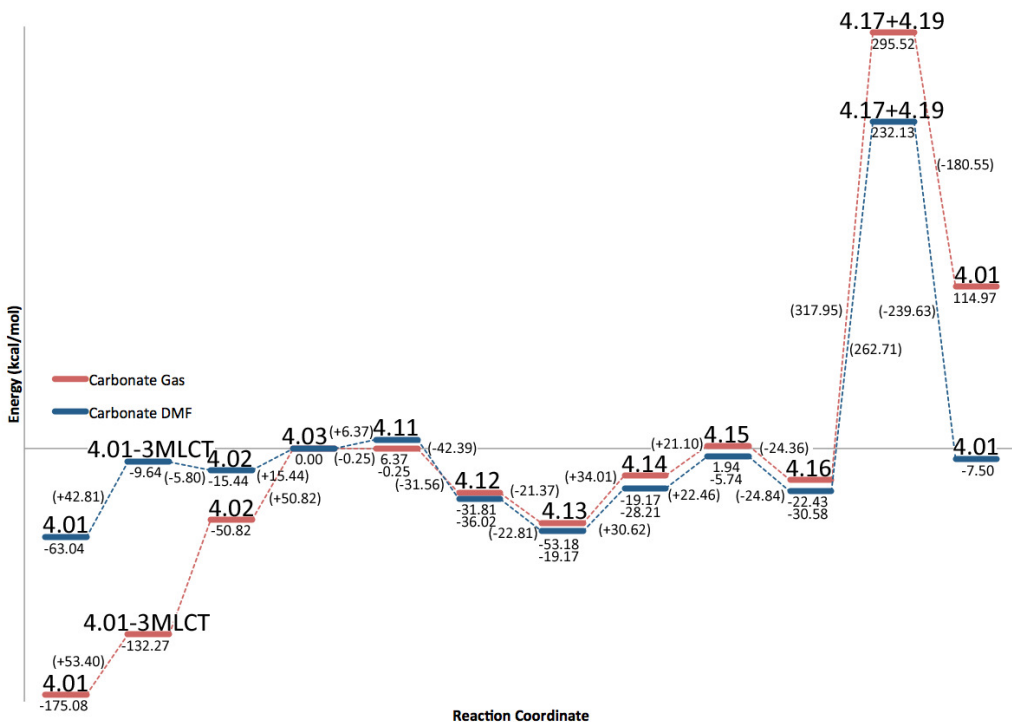


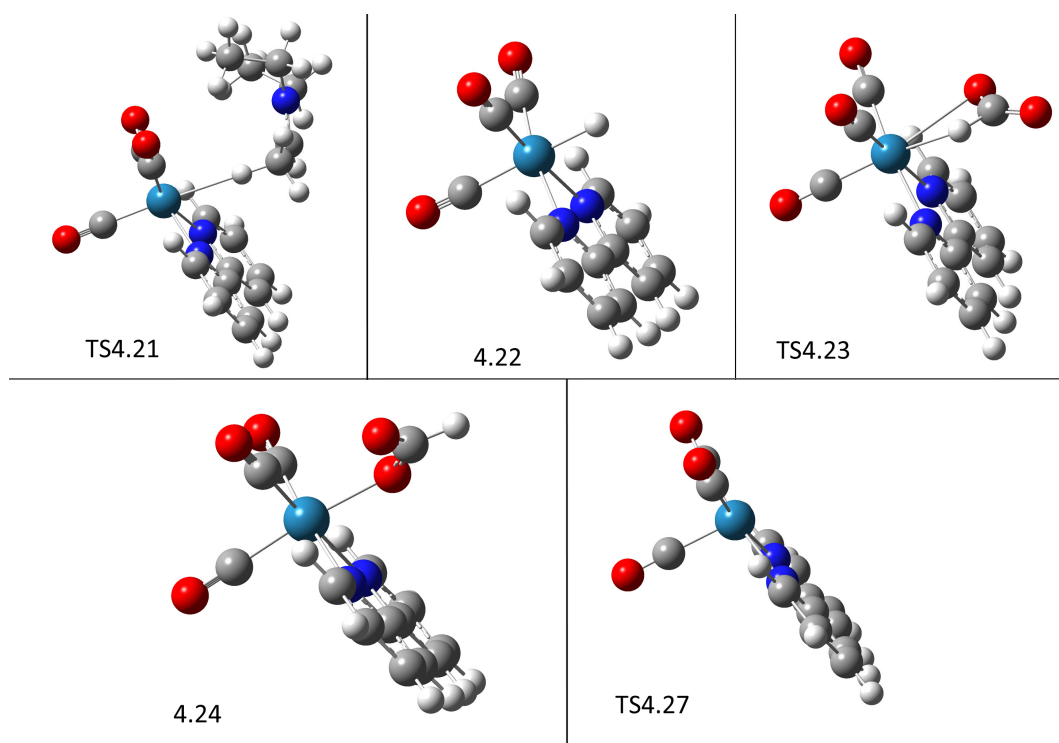
**Figure 4.3** Potential Energy Surface for the bicarbonate mechanistic pathway. Gas phase energies in red, DMF solvated energies in blue. A larger version is available in Appendix D, Figure D.7.

excimer to form a dimer **4.12**. This dimer formation is exothermic by 42.4 kcal/mol in DMF. The quenching of the radical forms much stronger bonds between the metal atoms and the linking CO<sub>2</sub>. The Re-C distance has shortened from the 2.51 Å seen in **4.11** to 2.26 Å. This is still longer than the Re-CO bonds, which is expected due to the lack of π back-bonding observed with carbonyl ligands, however, it corresponds with similar published crystal structures of Re-C bond lengths for sp<sup>2</sup> carbons.<sup>189</sup> The Re-O bond is 2.13 Å, a value that remains constant for Re-O through the intermediates in the reaction pathway.

After the dimer **4.12** has been formed, a second molecule of CO<sub>2</sub> is inserted via transition state **4.13** to form the Re-C(O)-O-C(O)-O-Re complex **4.14**. This C<sub>2</sub>O<sub>4</sub> linker

**Table 4.3** Energies for the reaction steps in the ‘formate’ pathway

Steps	Energy(gas) <sup>a</sup>	Energy(dmf) <sup>b</sup>
<b>4.03 + 4.07 → TS4.21</b>	20.99	20.87
<b>TS4.21 → 4.22 + 4.26</b>	-43.54	-50.72
<b>4.22 + 4.09 → TS4.23</b>	21.24	14.02
<b>TS4.23 → 4.24</b>	-33.94	-28.66
<b>4.24 → 4.25 + TS4.27</b>	140.39	39.67
<b>TS4.27 + 4.04 → 4.01</b>	-141.77	-36.37

<sup>a</sup> TPSS energy in kcal/mol.<sup>b</sup> TPSS energy in kcal/mol with COSMO solvation in DMF.**Figure 4.4** DFT calculated structures for the ‘formate’ mechanistic pathway. Atoms are coloured as follows: carbon - grey, nitrogen - blue, oxygen - red, hydrogen - white, rhenium - teal.

from the oxidized chain of the sacrificial amine **4.07** in transition state **4.21**, a step endothermic by 21.0 kcal/mol in the gas phase and 20.9 kcal/mol in DMF. The radical amine (**4.07**) had been previously formed (see subsection 4.2.1). Extraction of the proton

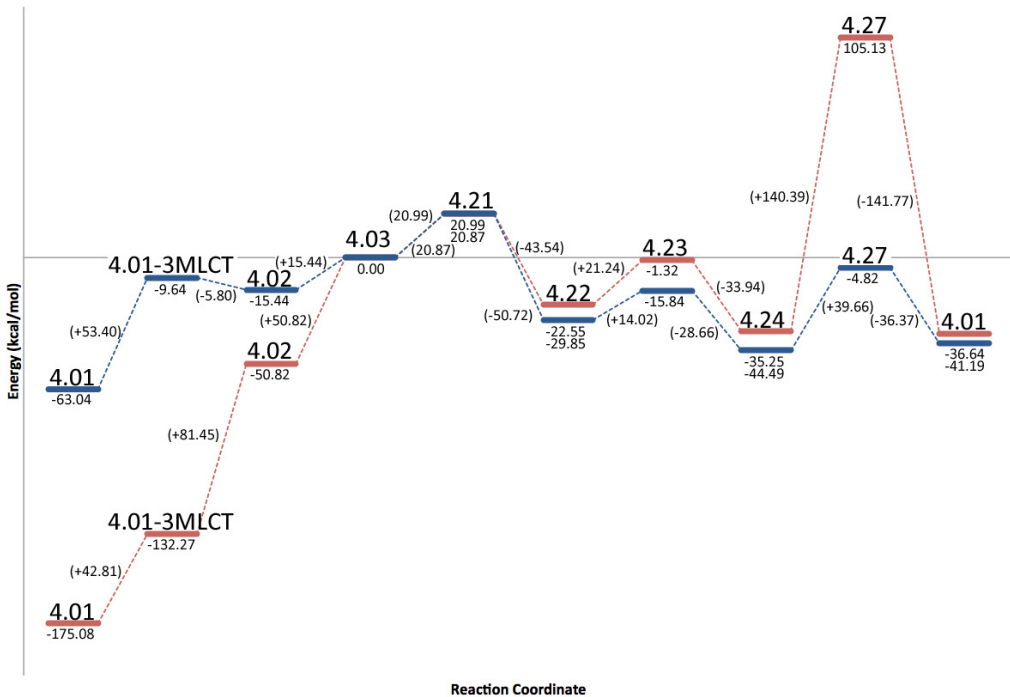
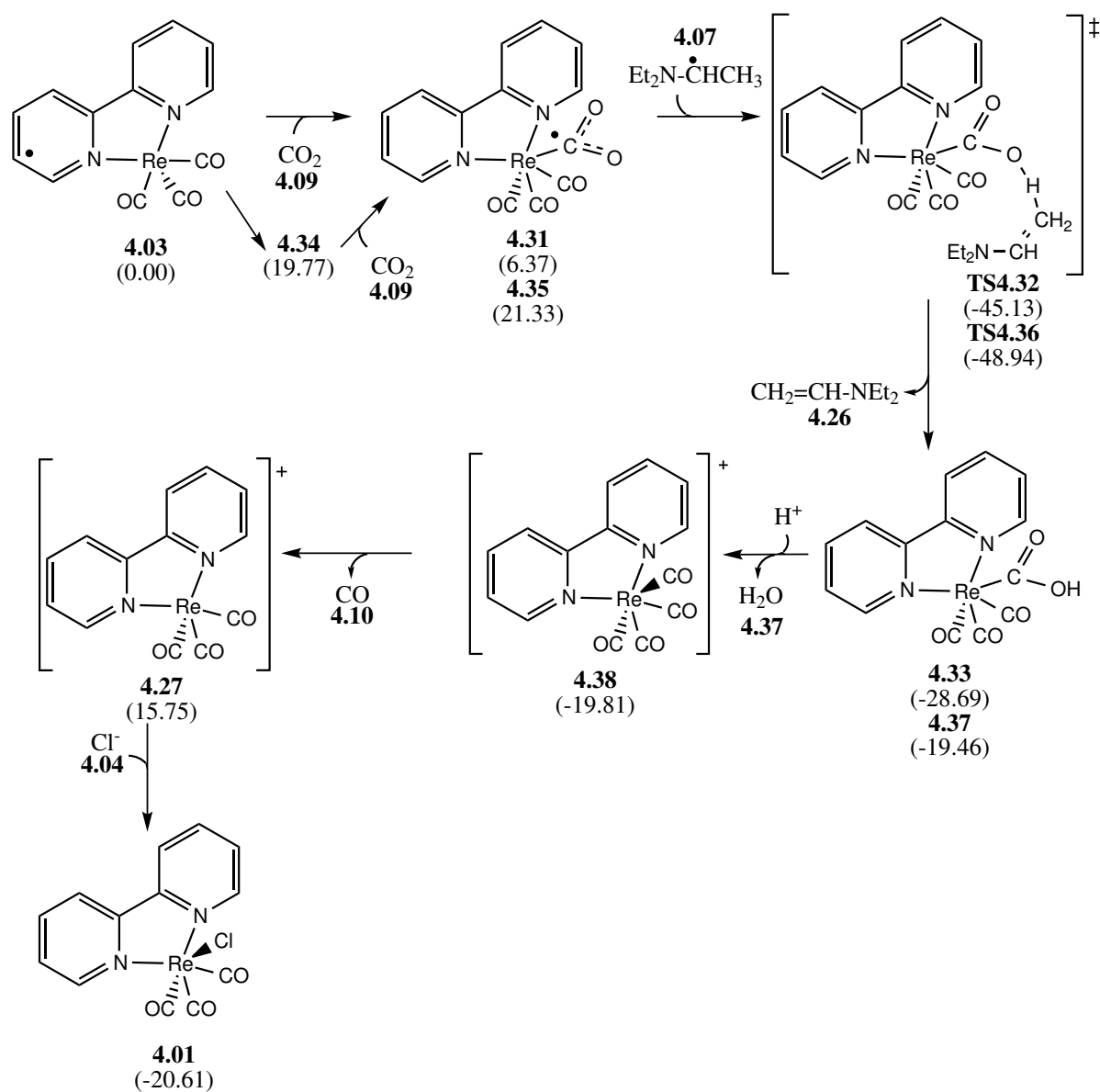


**Figure 4.5** Potential Energy Surface for the formate mechanistic pathway. Gas phase energies in red, DMF solvated energies in blue. A larger version can be seen in Appendix D, Figure D.6.

and electron pair allows for the formation of the ethene, completing the decomposition of the amine to the final neutral, singlet molecule **4.26**. Relaxation of this transition state results in the hydrogen extraction from the radical species, yielding the formation of the hydride complex **4.22**, a step exothermic by 50.7 kcal/mol in DMF.

This hydride complex is able to insert a molecule of CO<sub>2</sub> into the metal-hydrogen bond, in transition step **4.23**, with a 14.4 kcal/mol barrier to transition state formation. CO<sub>2</sub> insertion to metal hydrides is commonly observed, most mechanisms in CO<sub>2</sub> reduction in similar ruthenium systems employ this addition.<sup>193</sup> The Re-H bond length is 1.76 Å, compared to the length of the Re-Cl bond from the ground state **4.01** species of 2.51 Å. This bond length difference reflects the observations on anion change from Cl to Br (as discussed in chapter 2, subsection 2.3.2), the anion size is the critical factor



**Scheme 4.6** The ‘water-gas shift’ mechanistic pathway. Energy in kcal/mol relative to the excimer **4.03** is shown in brackets for each compound.

the ethene amine **4.26**. The newly formed acid species **4.32** dehydrates in the presence of a second proton (via **4.33**) to form water **4.37** and the tetracarbonyl cationic species **4.38**. This is endothermic by 8.9 kcal/mol in solution, but the  $\Delta G$  is -15 kcal/mol. This tetracarbonyl cation exchanges a CO molecule for a  $\text{Cl}^-$  to return to **4.01**, with a

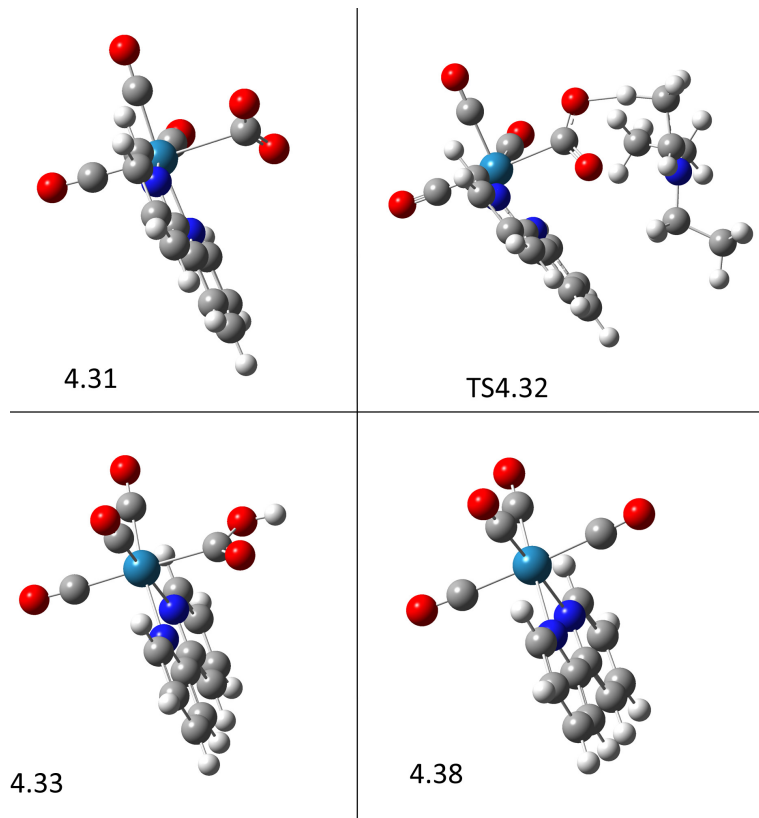


**Figure 4.6** DFT calculated structures for the axial ‘water-gas shift’ mechanistic pathway. Atoms are coloured as follows: carbon - grey, nitrogen - blue, oxygen - red, hydrogen - white, rhenium - teal.

0.8 kcal/mol energy release.

Typically, this reaction had been thought to proceed on the axial site of the catalyst, mirroring the pathways discussed above. However, due to the ease of migration of carbonyl groups in organometallic complexes, it is proposed that the ‘water-gas shift’ mechanism does not occur axial to the ligand, but begins with relocation of a CO<sub>2</sub> ligand to the axial position (see Scheme 4.7), followed by the coordination of CO<sub>2</sub> into the now vacant planar open site, forming **4.35**. Potential energies for this reaction are shown in Table 4.5, and the potential energy diagram is shown in Figure 4.9. DFT computed structures are shown in Figure 4.8.

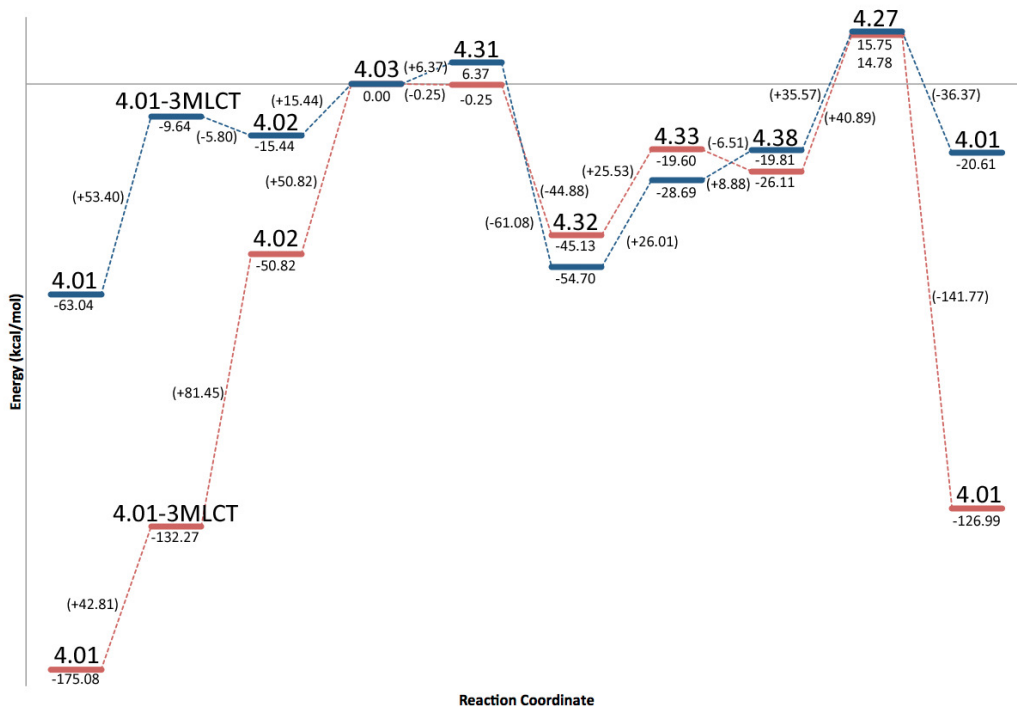
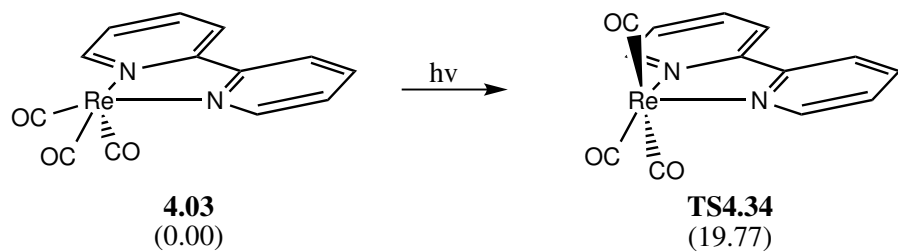


**Figure 4.7** Potential Energy Surface for the axial geometry of the water-gas shift mechanistic pathway. Gas phase energies in red, DMF solvated energies in blue. A larger version can be seen in Appendix D, Figure D.3.

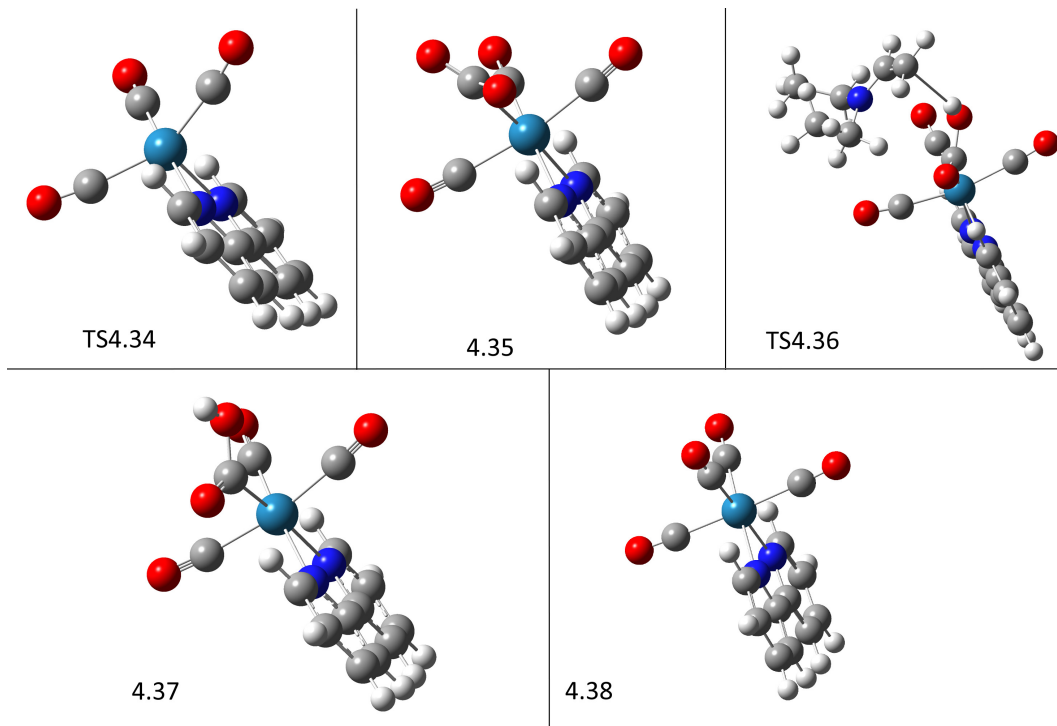


**Scheme 4.7** Rearrangement of carbonyl and open site. Energy in kcal/mol relative to the excimer **4.03** is shown in brackets for each compound.

This  $\text{CO}_2$  bound in the plane of the ligand then undergoes hydrogen addition and dehydration to produce a molecule of  $\text{H}_2\text{O}$ , continuing as before. Once reduced to the tetracarbonyl cluster, the catalyst could shed any CO ligand and pick up a chloride anion to return to the neutral ground state. However, labilization of one of the two axial

**Table 4.5** Energies for the reaction steps in the ‘equatorial’ geometry

Steps	Energy(gas) <sup>a</sup>	Energy(dmf) <sup>b</sup>
<b>4.03 → TS4.34</b>	23.37	19.77
<b>TS4.34 + 4.09 → 4.35</b>	4.79	1.56
<b>4.35 + 4.07 → TS4.36</b>	-36.36	-49.13
<b>TS4.36 → 4.37 + 4.26</b>	-3.39	8.34
<b>4.37 → 4.38 + 4.39</b>	-14.52	-0.35
<b>4.38 → 4.27 + 4.10</b>	40.89	35.57
<b>4.27 + 4.04 → 4.01</b>	-141.77	-36.37

<sup>a</sup> TPSS energy in kcal/mol.<sup>b</sup> TPSS energy in kcal/mol with COSMO solvation in DMF.**Figure 4.8** DFT calculated structures for the equatorial ‘water-gas shift’ mechanistic pathway. Atoms are coloured as follows: carbon - grey, nitrogen - blue, oxygen - red, hydrogen - white, rhenium - teal.

carbonyls is the most favoured, formation of the planar coordinated chloride complex is not expected.<sup>180</sup>

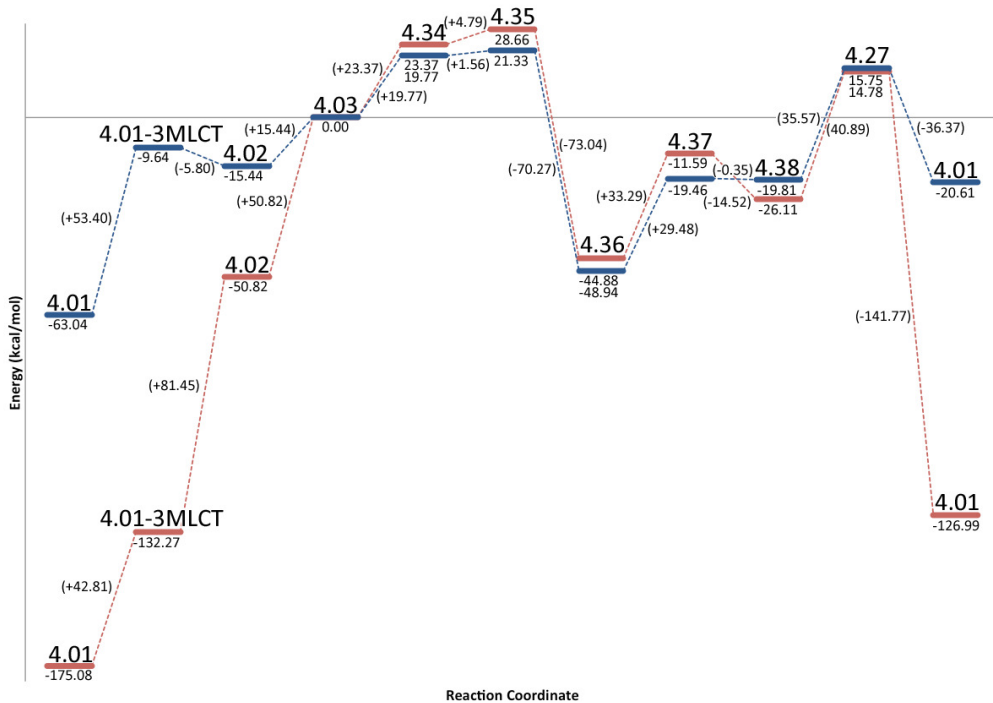


**Figure 4.9** Potential Energy Surface for the planar geometry of the water-gas shift mechanistic pathway. Gas phase energies in red, DMF solvated energies in blue. A larger version can be seen in Appendix D, Figure D.4.

This newly proposed mechanism provides an explanation to a previously unexplained phenomenon. The exchange of carbonyl groups on the catalyst for  $^{13}\text{CO}$  when using  $^{13}\text{CO}_2$  in the photoreduction is documented as early as Hawecker *et al.* in 1986.<sup>67</sup> It was shown that complete exchange occurs with very few catalytic turnovers. Furthermore, Koike *et al.* demonstrated that photochemical ligand substitution occurs at only axial sites relative to the  $\alpha$ -imino ligand,<sup>156</sup> no exchange occurs at the equatorial site, nor can the *fac*- $(^{12}\text{CO})_2^{13}\text{CO}$  be expected to shift the  $^{13}\text{CO}$  to the equatorial position in the time-frame of the reaction. Thus the isotopic exchange does not proceed by independent uptake of produced  $^{13}\text{CO}$ , instead the conversion to the  $^{13}\text{CO}$  complex must be inherent in the reduction mechanism.

This modified geometry does not violate any previously published experimental mechanism work. These studies typically focus on photophysical or spectroscopic analysis to determine intermediates. The analysis methods used define molecular composition; they are not structural characterization techniques. Re-evaluation of the spectral data within these newly defined parameters does not invalidate the work, mechanistic descriptors published (such as kinetics) are still valid within the new geometry.

Additionally, this provides an explanation for the lack of CO<sub>2</sub> reduction by (terpy)- $\kappa^2$ -Re(CO)<sub>3</sub>Cl discussed in chapter 3. While the carbonyl group is transitioning to the axial site, before a molecule of CO<sub>2</sub> has been coordinated to the complex, the catalyst is in optimal geometry for chelation of the pendant arm (see Scheme 3.1) as discussed in chapter 3. It was previously shown that the tridentate catalyst is inactive for CO<sub>2</sub> photoreduction, the formation of a  $\kappa^3$  complex modifies the photophysics, deactivating the catalyst's reactivity.

### 4.3 Comparison Between Mechanistic Pathways

Previous studies in literature had only analyzed one of the mechanistic pathways (or a subset), without a fuller analysis of the competitiveness of each pathway relative to the others. Discussion on the tenability of each potential pathway relied on the *in situ* observation of intermediates or transition states, the success (or lack thereof) of synthesis of the intermediates, and the relative production of by-products in the mechanistic trials.

The overall potential energy diagrams for each of the mechanistic pathways given in Scheme 4.1 are shown in Figure 4.10. Individual mechanistic pathways, and separate potential energy diagrams for gas phase and DMF solvated structures are listed in Appendix D. This figure shows the difficulty in determining the most likely reaction pathway based on computational analysis alone. The difference in energy consumption between

mechanisms is quite small, with the largest barriers belonging to the final disassociation of the product and coordination of chloride.

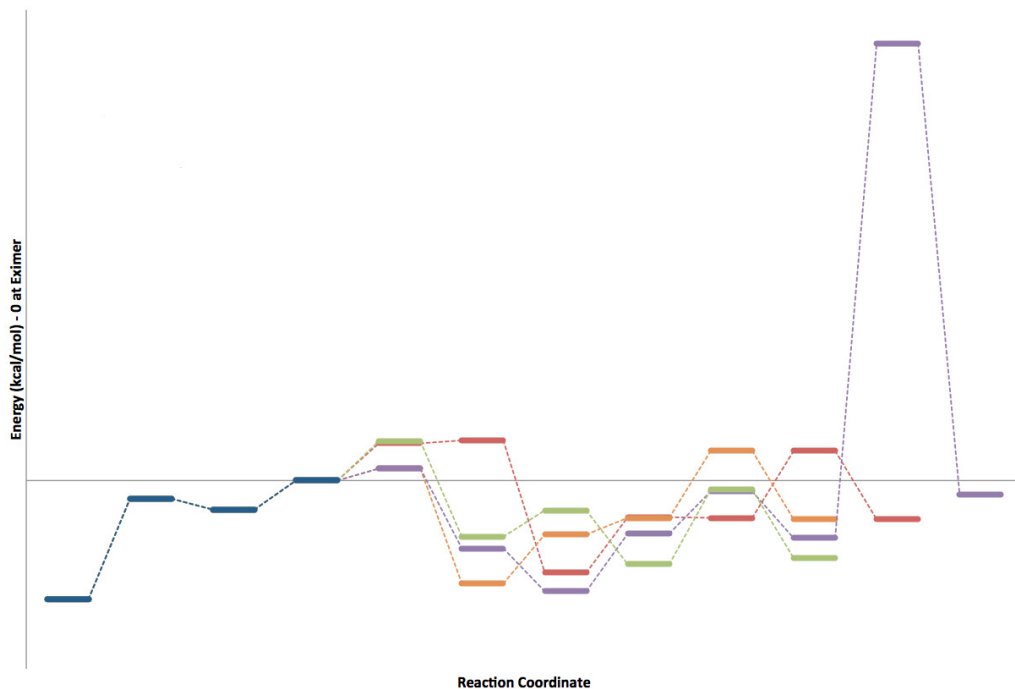


**Figure 4.10** An overview of the energies of the three mechanistic pathways of photochemical  $\text{CO}_2$  reduction in DMF. Excimer formation is shown in blue, the planar water-gas shift mechanism in red, the axial water-gas shift in orange, the bicarbonate in purple, and the formate in green.

Experimental data shows that each of the mechanisms is feasible and could occur in certain conditions. Both the formate and water-gas routes have the maximum transition energy barrier for the final disassociation of the product and coordination of chloride. This barrier is artificially high, the charge separation that occurs is impacted significantly by the basic pH and the presence of electrolyte in solution experimentally. These factors are not taken into consideration in the calculations. Gibbs energies were calculated for these steps, the average  $\Delta G$  values are around -12 kcal/mol for the production of the transition state, signifying a thermodynamically favoured reaction.

Due to the similarity in potential energy profiles for these reactions, analysis of experimental data must be undertaken to accurately predict which pathway dominates the photoreduction of CO<sub>2</sub>. The energy requirements of each pathway is not the only indicator of mechanistic preference. Studies have shown the rate differs between pathways, with the formation of certain intermediates being so slow as to nearly block the progression of the redox reaction. Utilization of modified reaction conditions (TEA vs. TEOA, changing solvent mixture, presence or absence of H<sub>2</sub>O, presence or absence or modification of electrolyte) can provide a range of reduction products, by-products, and intermediates.<sup>66,67,70,87,129,147</sup>

## 4.4 Conclusions

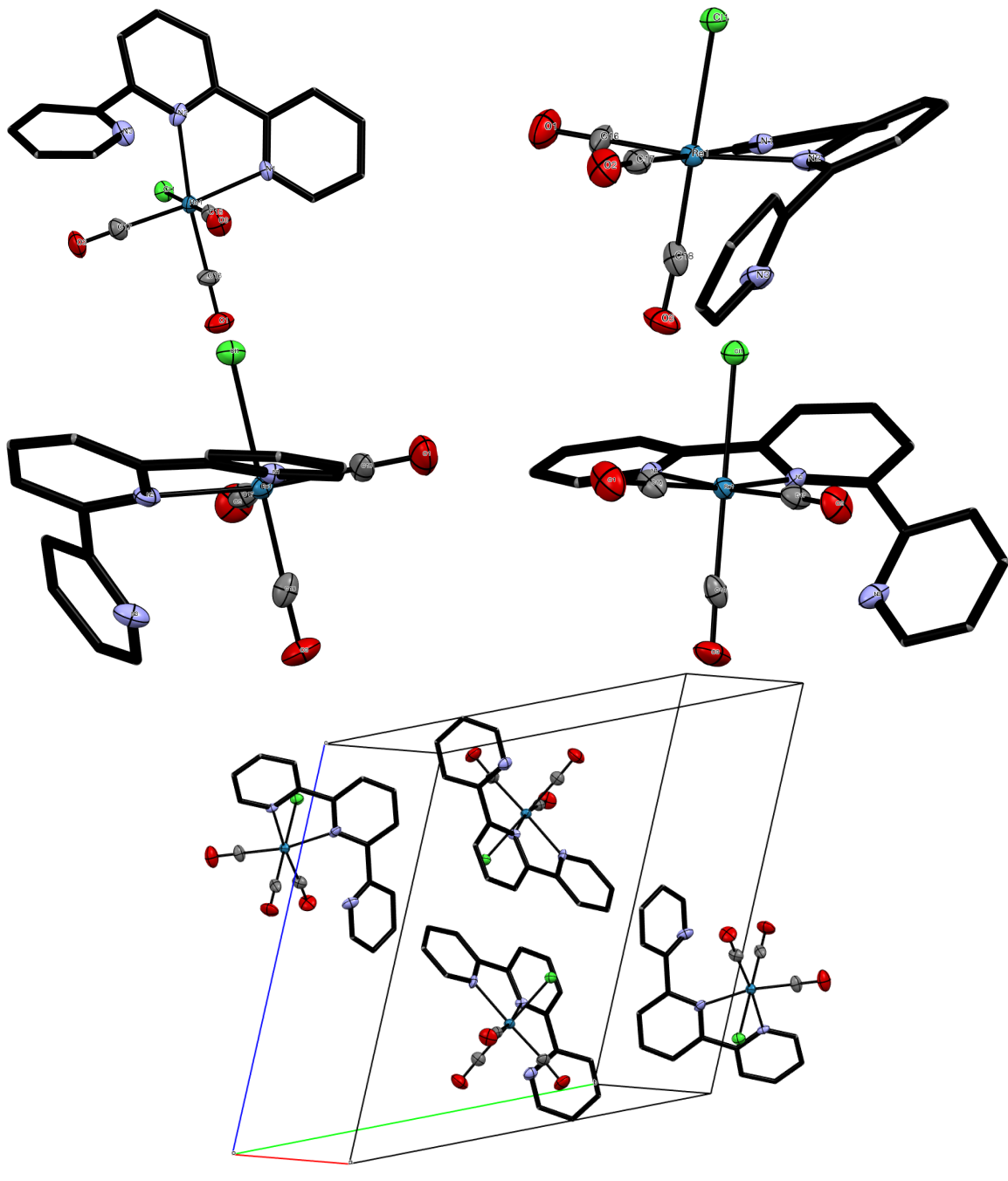
Three feasible mechanistic pathways for the photocatalytic reduction of CO<sub>2</sub> were investigated in detail using consistent DFT methods, allowing for their comparison. Mechanistic steps not previously elucidated were demonstrated, showing the full mechanistic cycle from ground state excitation through the reaction of the excimer with CO<sub>2</sub> to the final release of product and reforming of catalyst.

A modified geometry for the production of CO and H<sub>2</sub>O by the ‘water-gas’ mechanism was proposed. This new geometry does not conflict with previously published experimental data, and provides explanation for previously reported phenomenon. It aligns with the previously demonstrated inactivity of terpyridine catalysts, in contrast to the highly active bipyridine analogue. This new geometry provides an avenue for the isotopic exchange of carbonyl ligands from <sup>12</sup>CO to <sup>13</sup>CO when the reduction is carried out with <sup>13</sup>CO<sub>2</sub>.

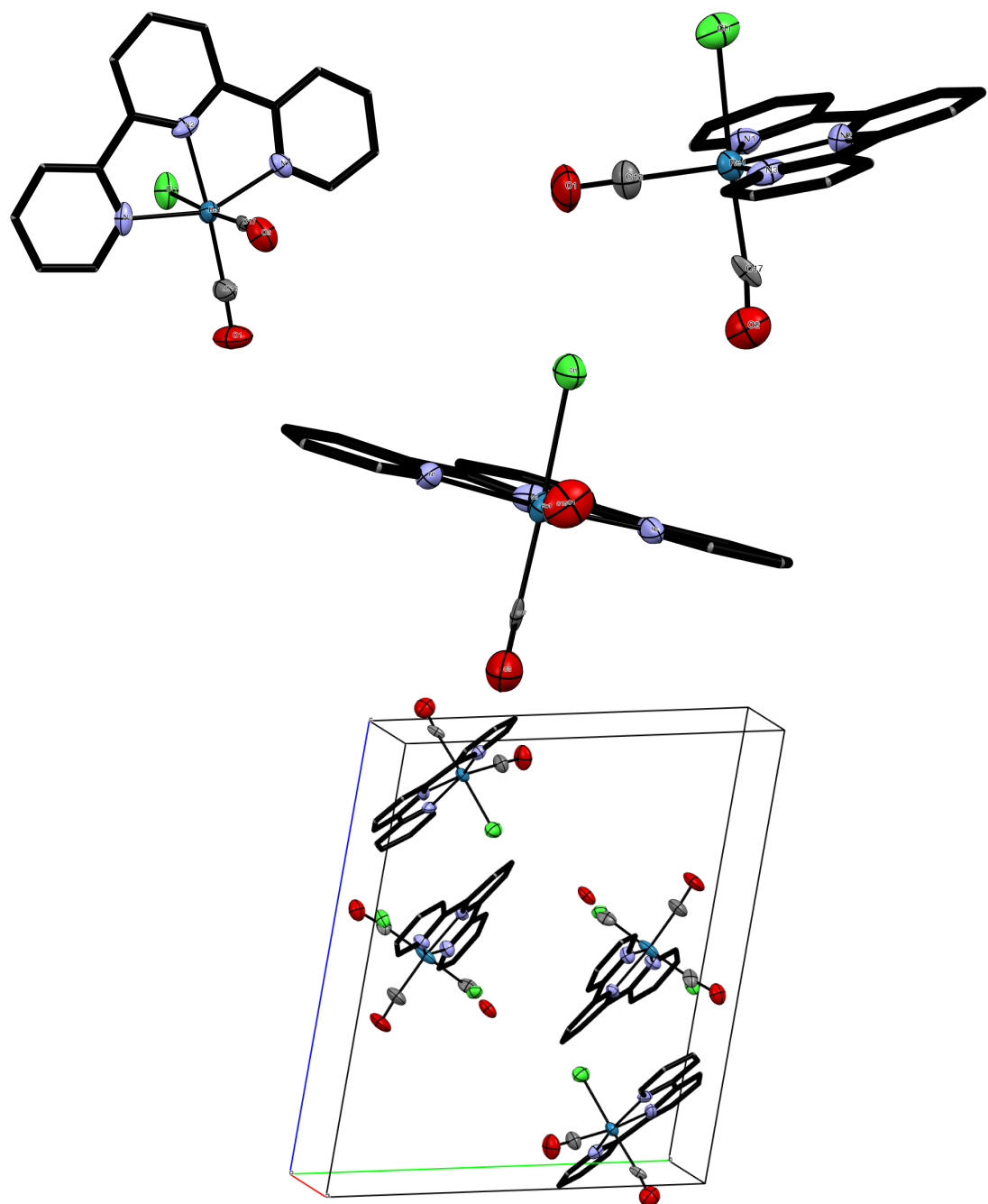
## **Appendix B**

### **X-ray Crystal Structures**

Multiple views of each x-ray crystal structure (including full unit cell) as discussed in chapter 2 are shown in Figures B.1 to B.5.

(a) Full unit cell representation of **2.1**.

**Figure B.1** X-ray crystal structure of **2.1**. Co-crystallized chloroform, hydrogen atoms, and thermal ellipsoids of ligand carbon atoms are omitted for clarity.

(a) Full unit cell representation of **2.2**.

**Figure B.2** X-ray crystal structure of **2.2**. Co-crystallized chloroform, hydrogen atoms, and thermal ellipsoids of ligand carbon atoms are omitted for clarity.

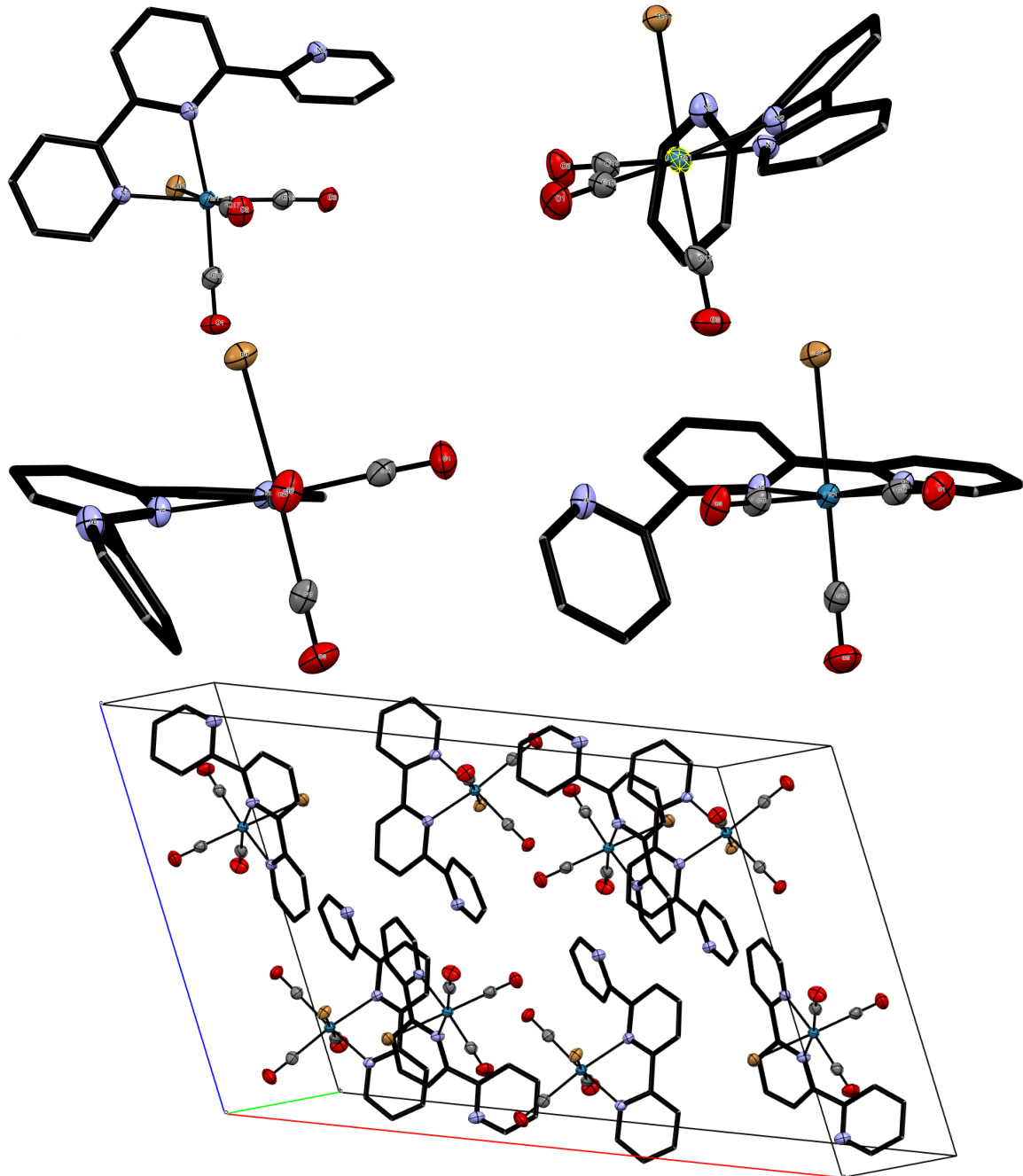


**Figure B.3** X-ray crystal structure of **2.3**. Hydrogen atoms, and thermal ellipsoids of ligand carbon atoms are omitted for clarity.

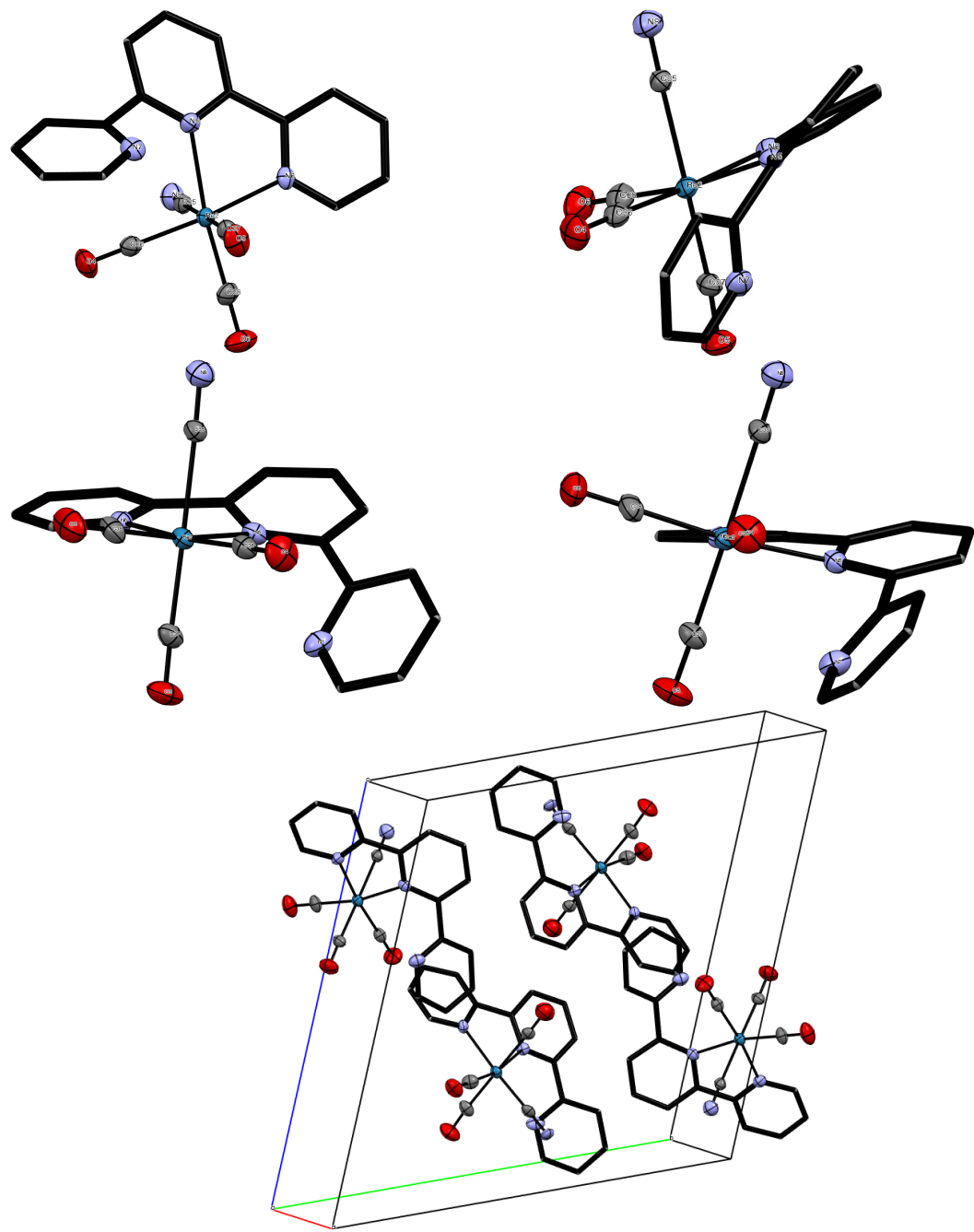


**Figure B.4** X-ray crystal structure of **2.5**. Hydrogen atoms, and thermal ellipsoids of ligand carbon atoms are omitted for clarity.

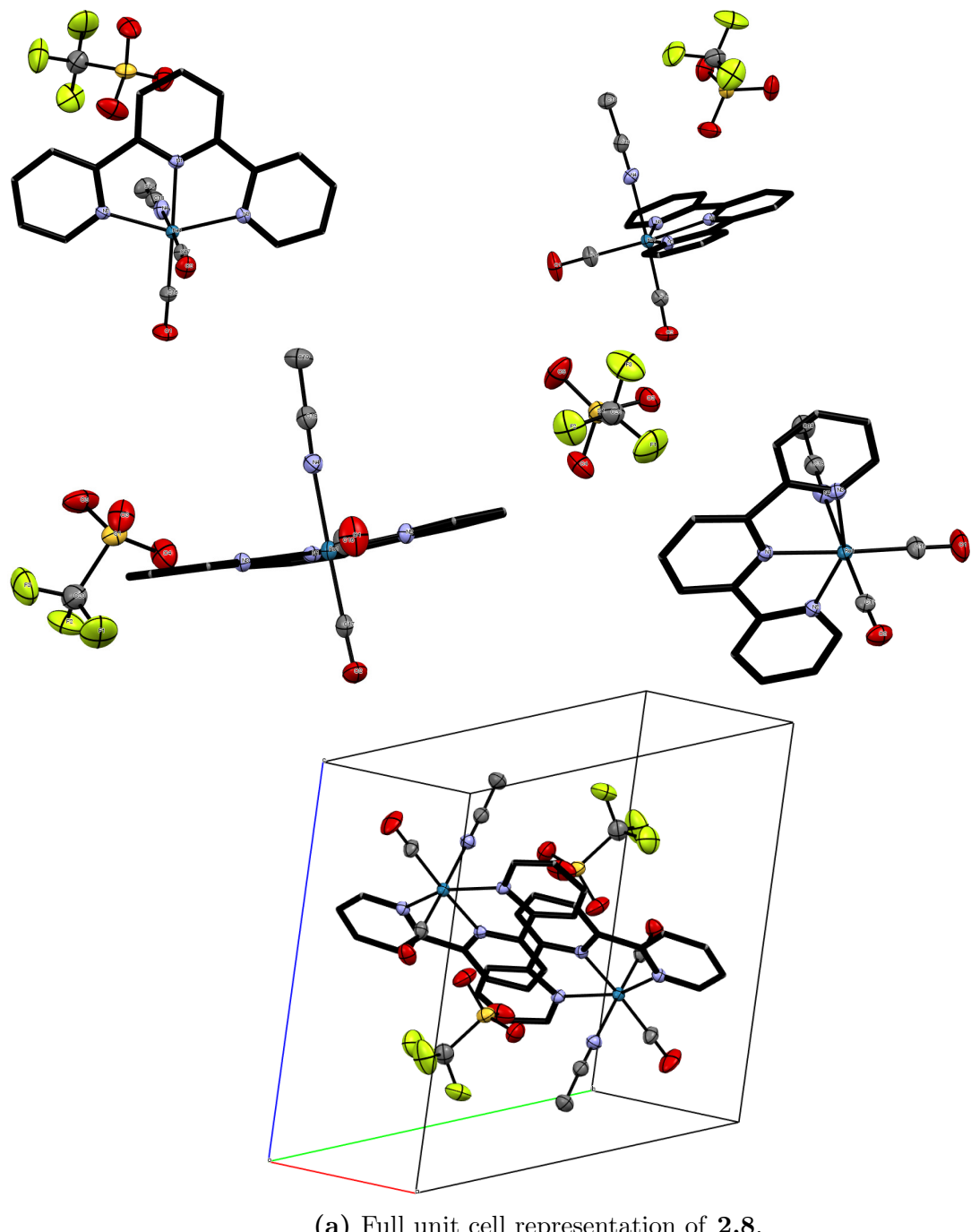


**Figure B.5** X-ray crystal structure of **2.8**. Hydrogen atoms, and thermal ellipsoids of ligand carbon atoms are omitted for clarity.

## Appendix C

### Molecular Orbitals Diagrams

Frontier Molecular Orbitals (MOs) for each compound discussed in this thesis are listed below in Figures C.1 to C.8. These orbitals are generated with the Chemissian program<sup>203</sup> from the output of calculations performed in Gaussian 09.<sup>135</sup>

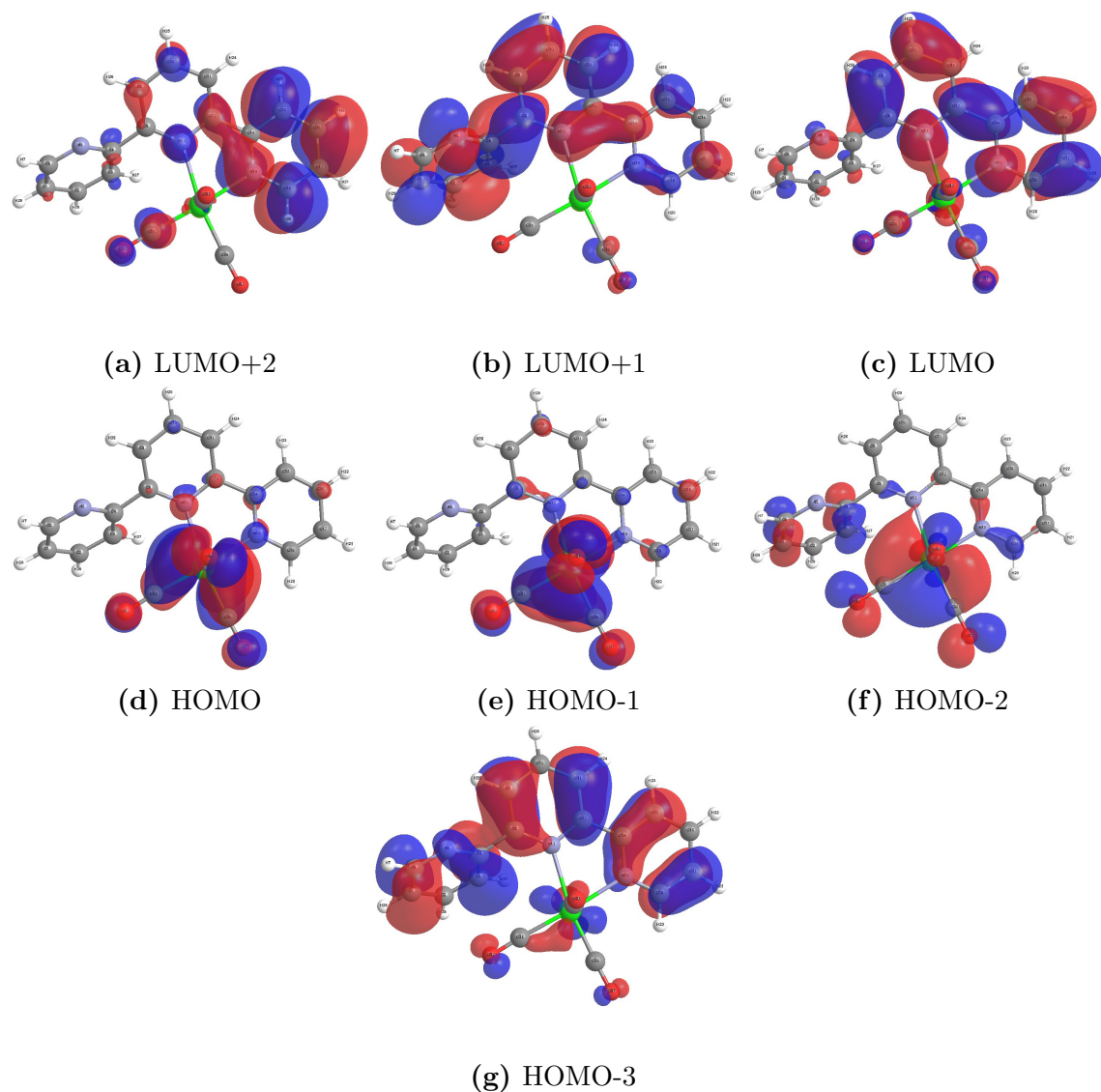


**Figure C.1** Isosurface plots of the frontier molecular orbitals HOMO-3 to LUMO+2 of **2.1**.

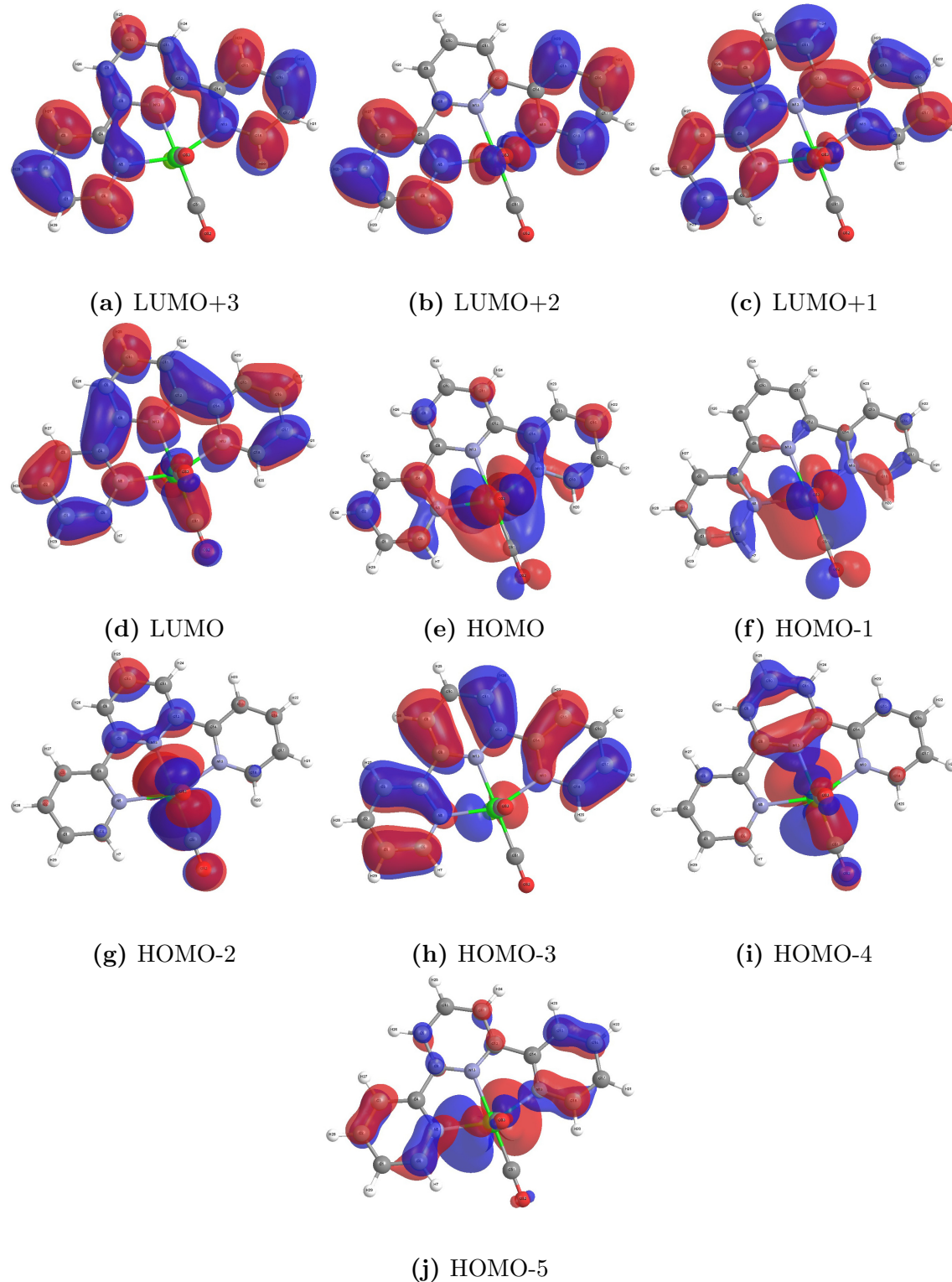


**Figure C.2** Isosurface plots of the frontier molecular orbitals HOMO-5 to LUMO+3 of **2.2**.

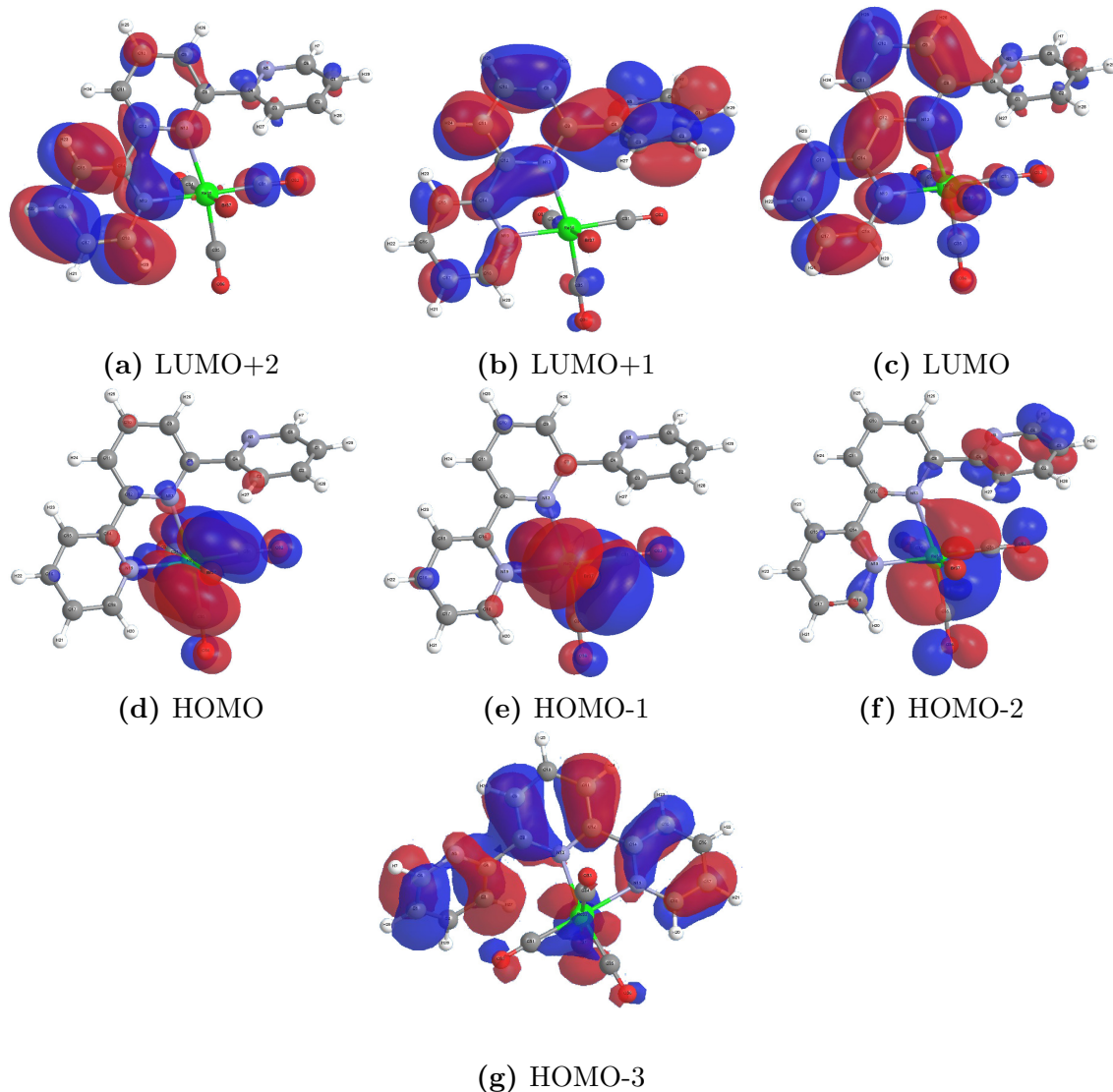


**Figure C.3** Isosurface plots of the frontier molecular orbitals HOMO-3 to LUMO+2 of 2.3.

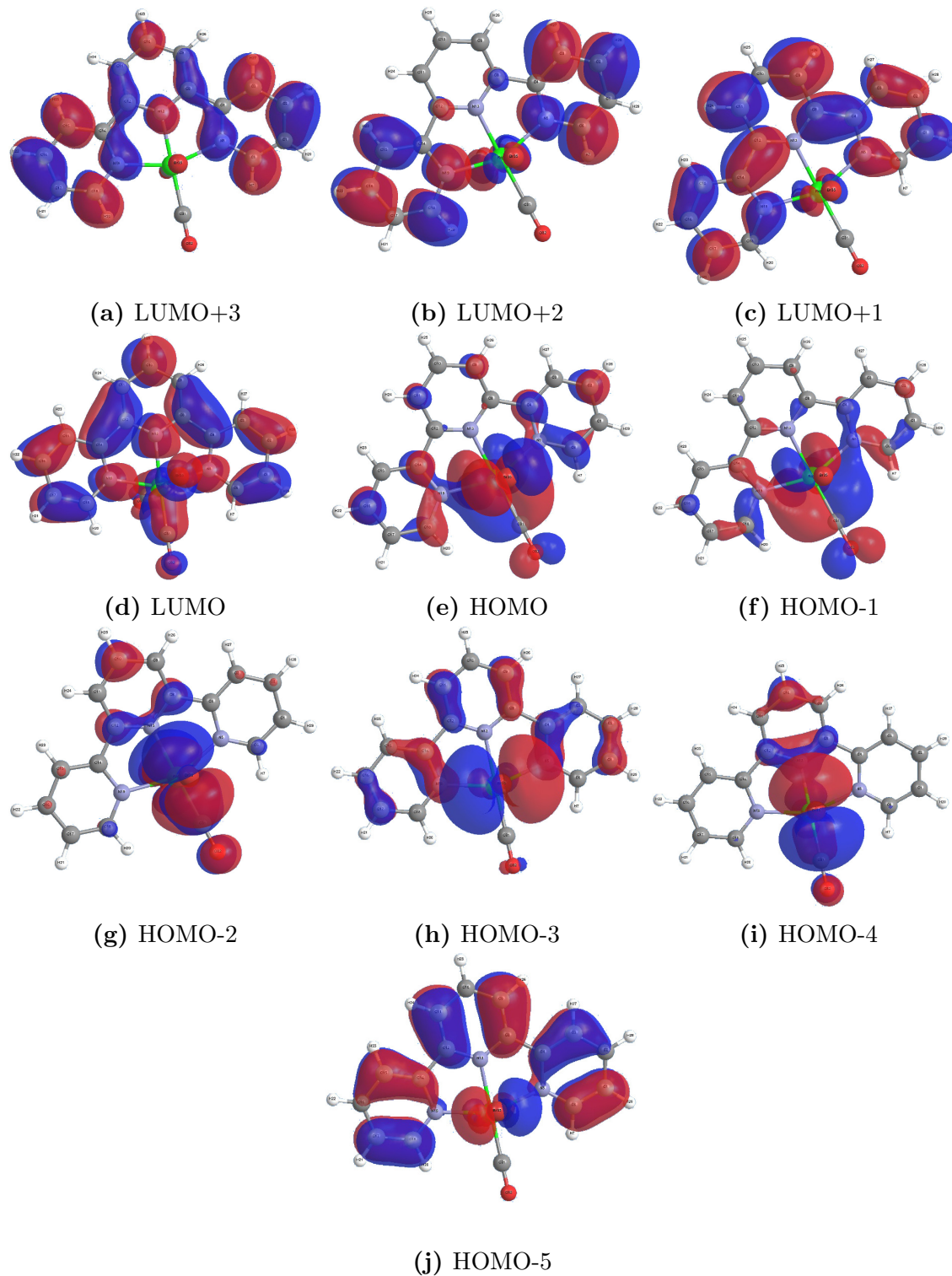


**Figure C.4** Isosurface plots of the frontier molecular orbitals HOMO-5 to LUMO+3 of 2.4.

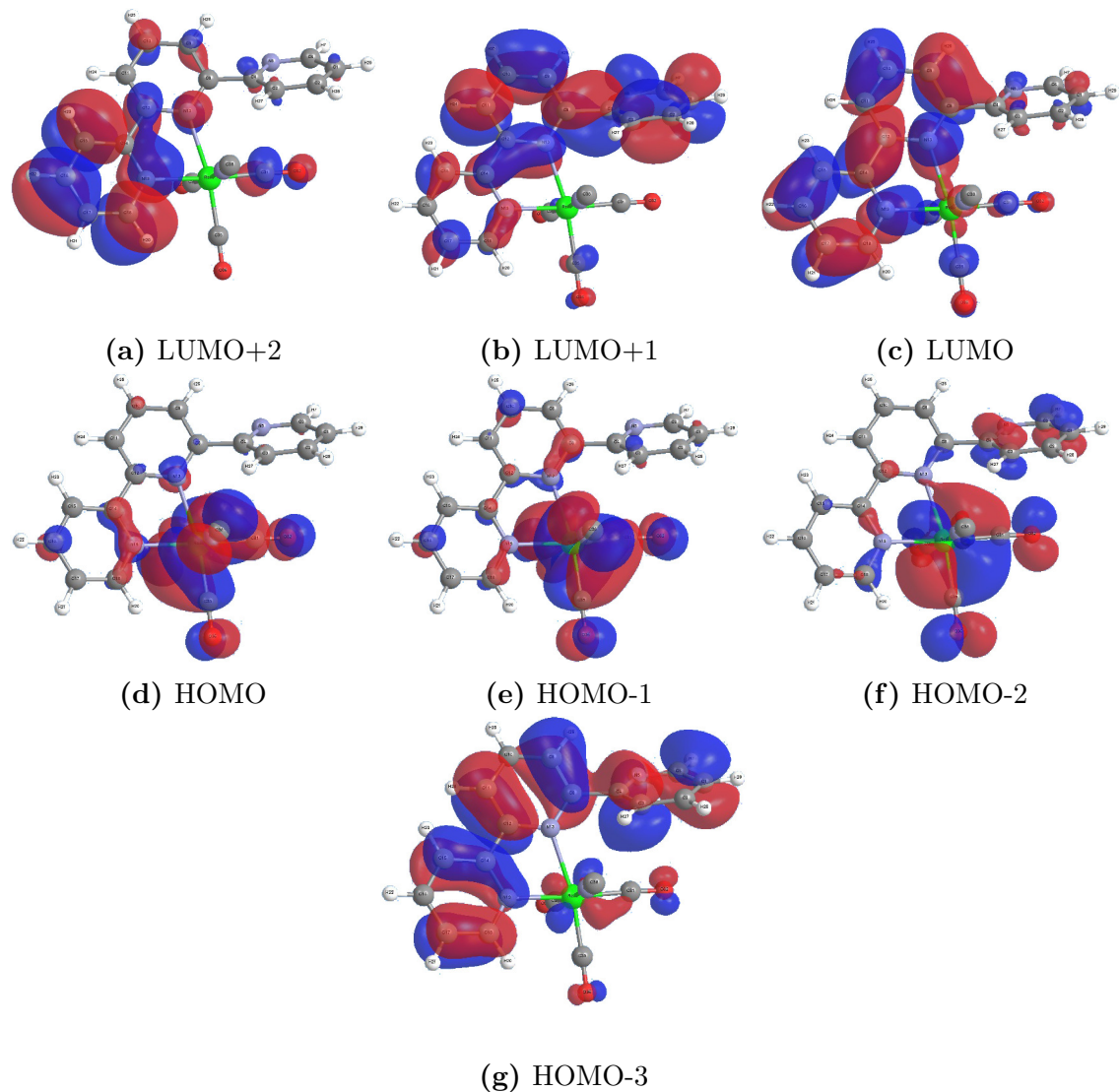


**Figure C.5** Isosurface plots of the frontier molecular orbitals HOMO-3 to LUMO+2 of 2.5.

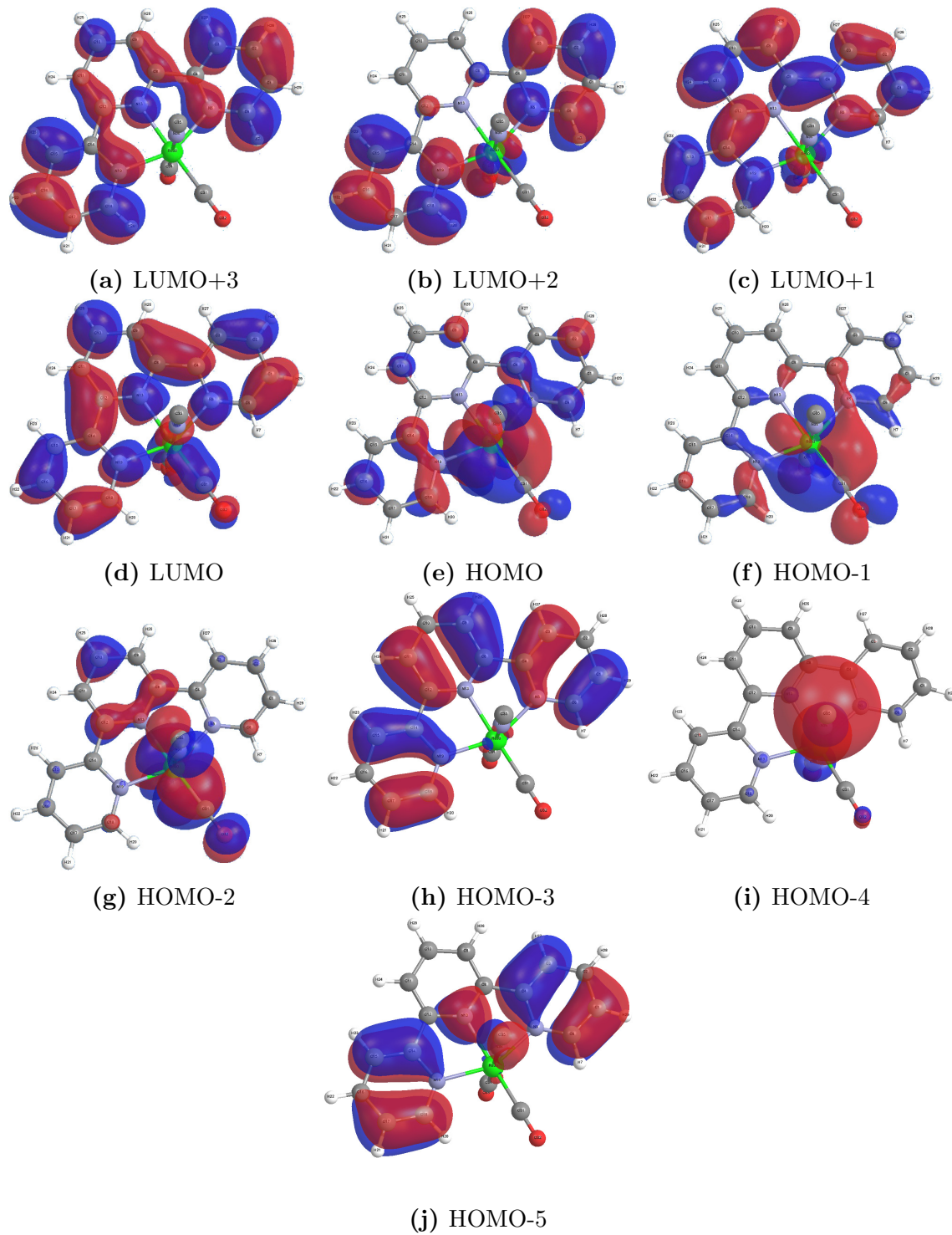


**Figure C.6** Isosurface plots of the frontier molecular orbitals HOMO-5 to LUMO+3 of 2.6.

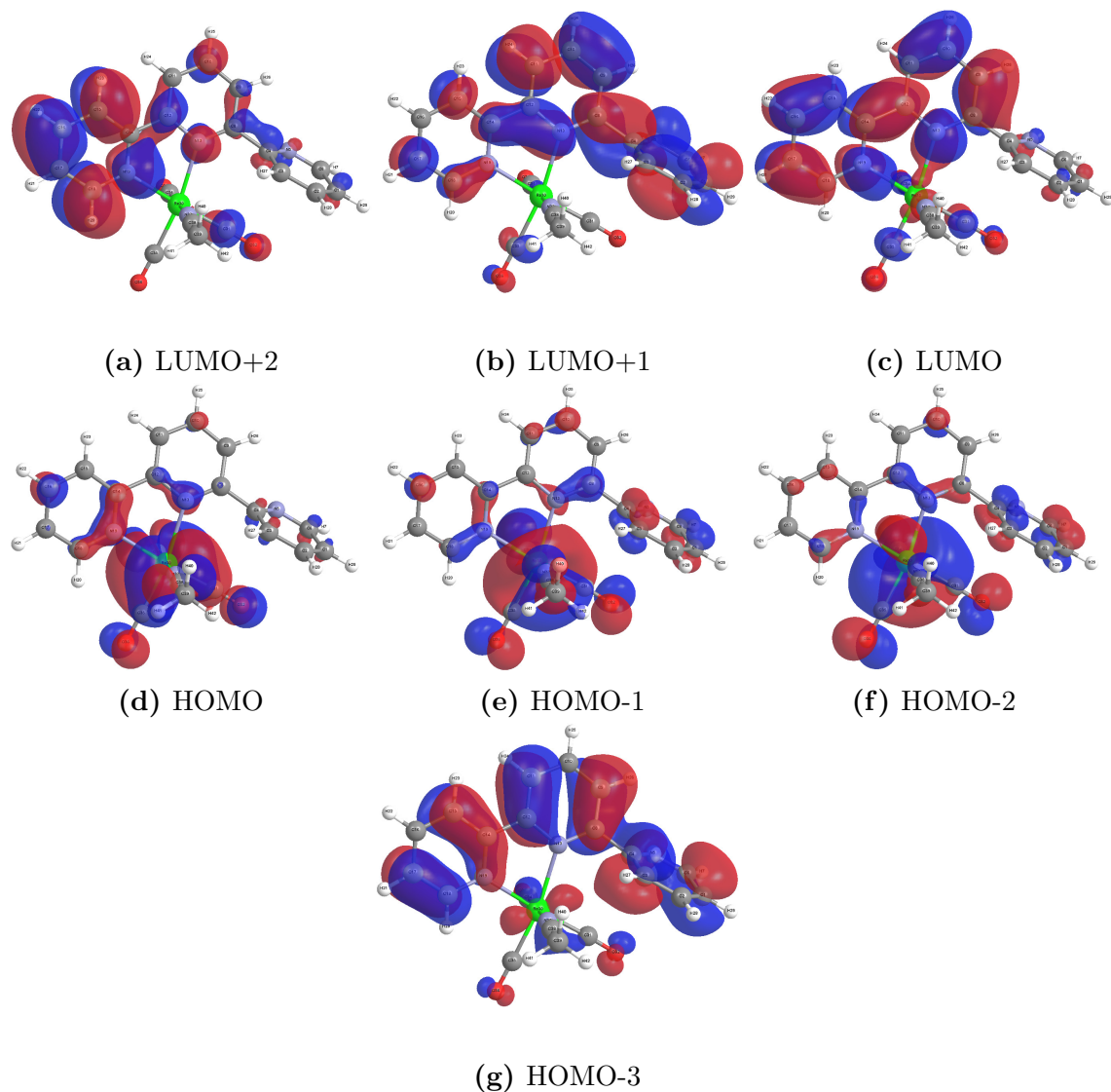


**Figure C.7** Isosurface plots of the frontier molecular orbitals HOMO-3 to LUMO+2 of 2.7.

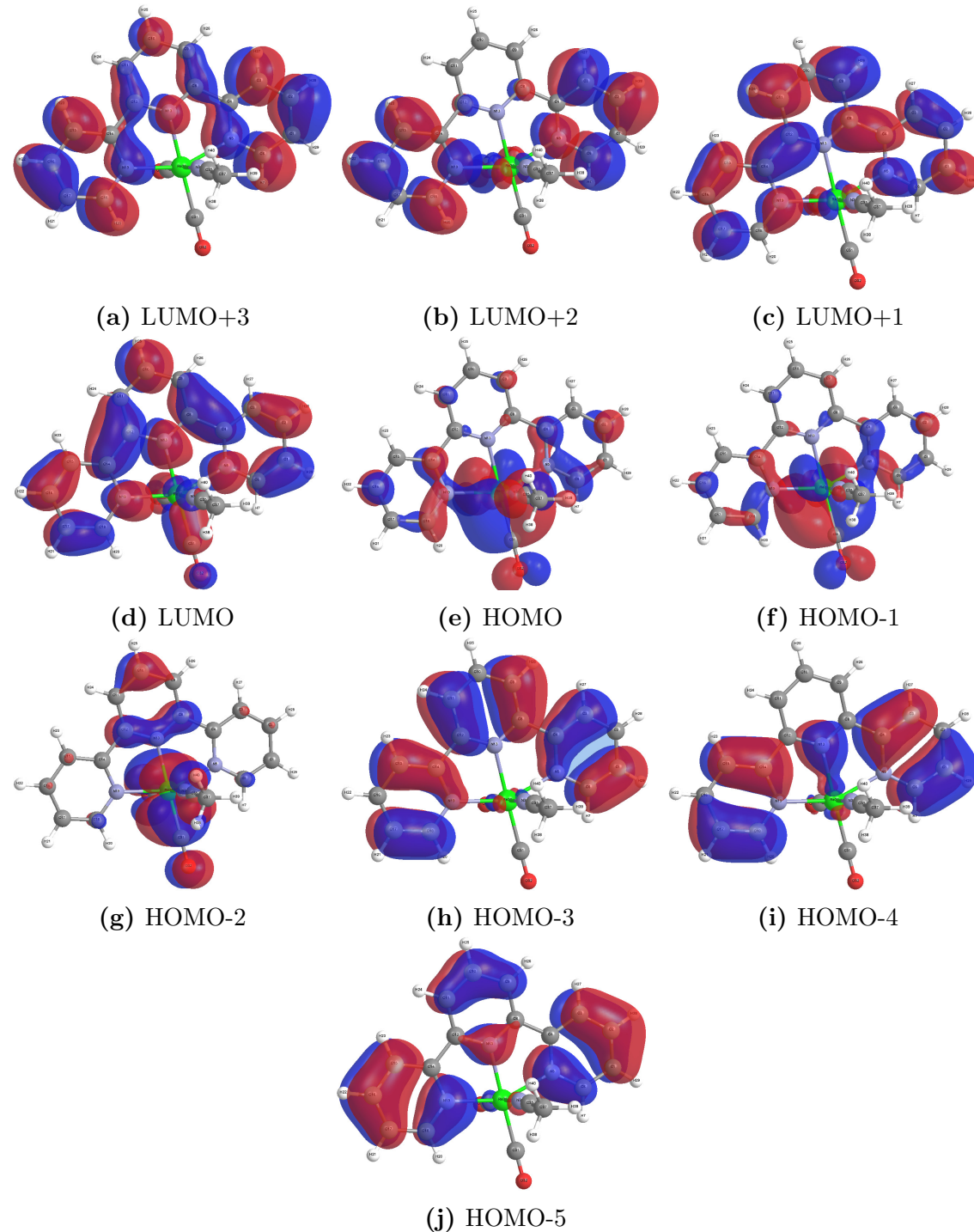


**Figure C.8** Isosurface plots of the frontier molecular orbitals HOMO-5 to LUMO+3 of **2.8**.



## **Appendix D**

### **Reaction Potential Energy Diagrams**

Potential energy diagrams for the reactions discussed in chapter 4 are listed below in Figures D.1 to D.9.

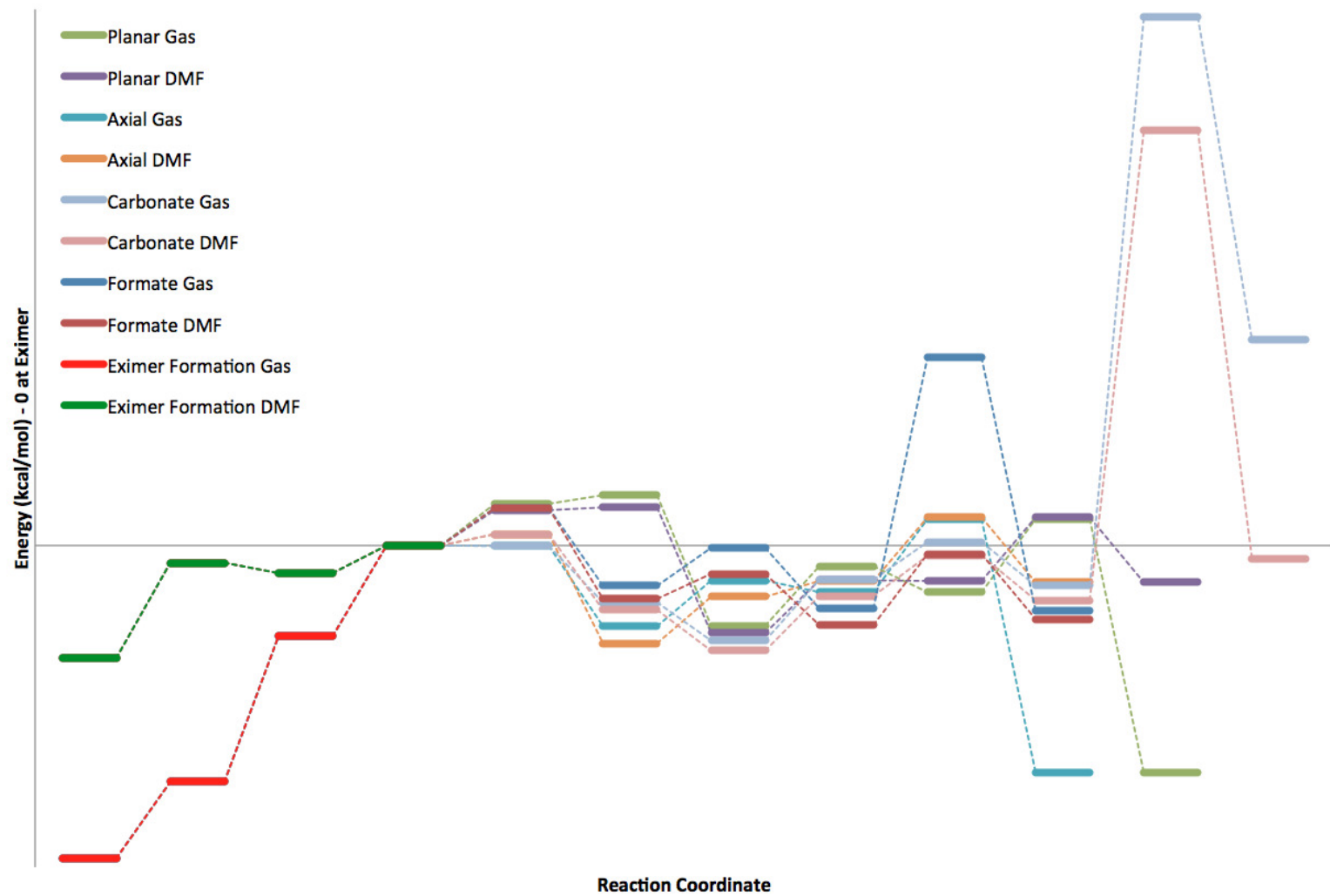


**Figure D.1** An overview of the energies of the three mechanistic pathways of photochemical  $\text{CO}_2$  reduction.

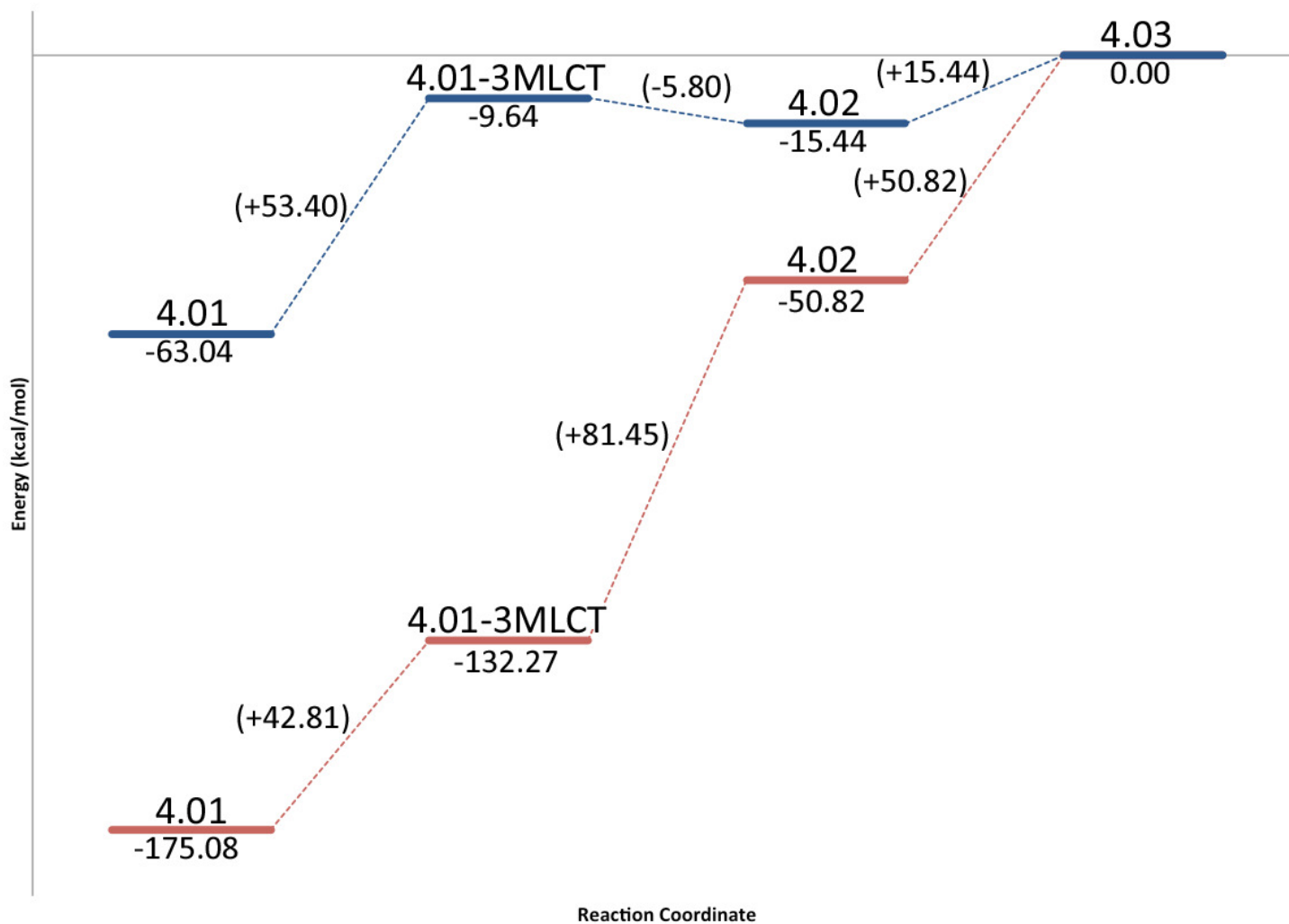


**Figure D.2** Potential Energy Surface for the production of the excimer. Gas phase energies in red, DMF solvated energies in blue.

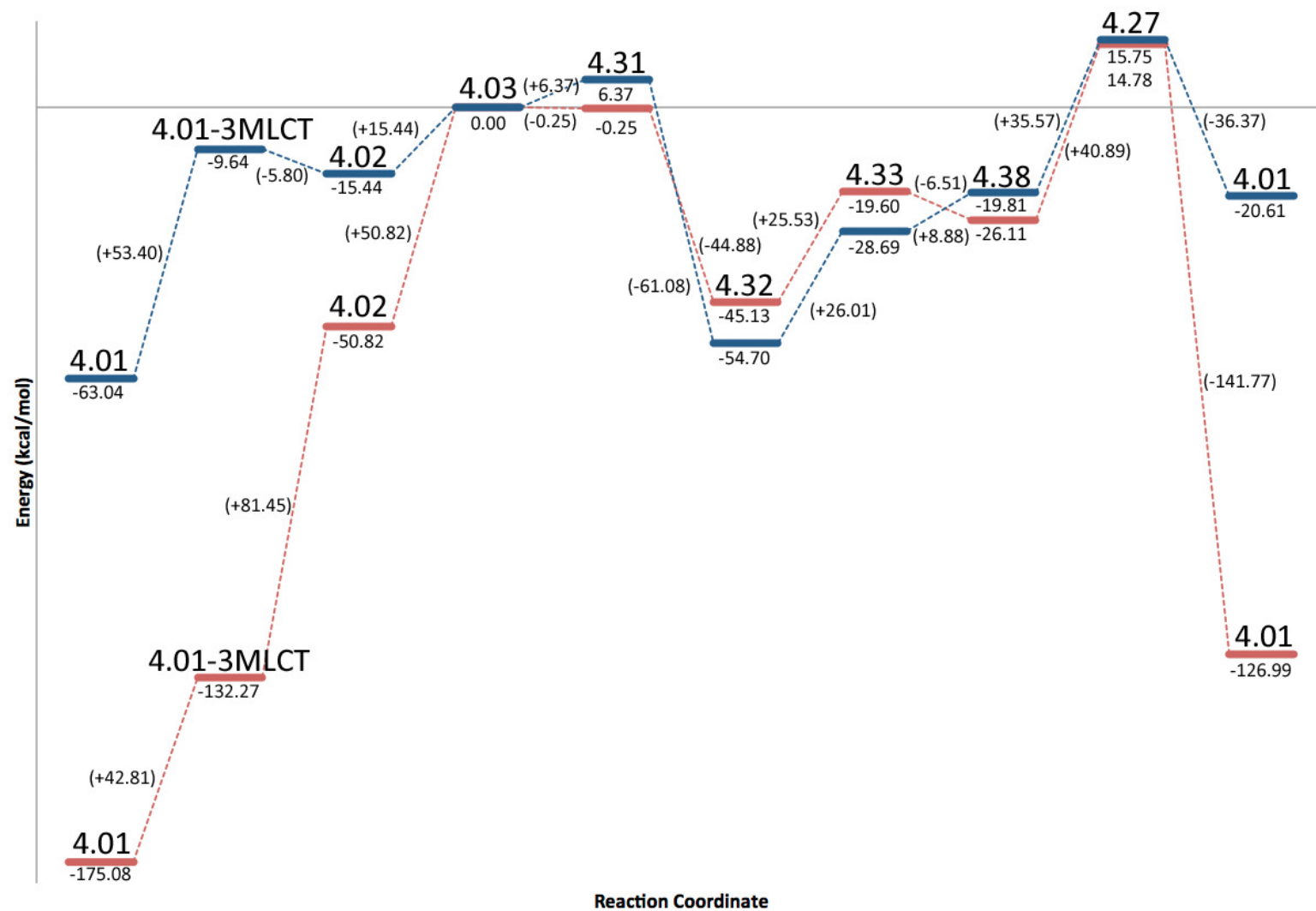


**Figure D.3** Potential Energy Surface for the axial geometry of the water-gas shift mechanistic pathway. Gas phase energies in red, DMF solvated energies in blue.

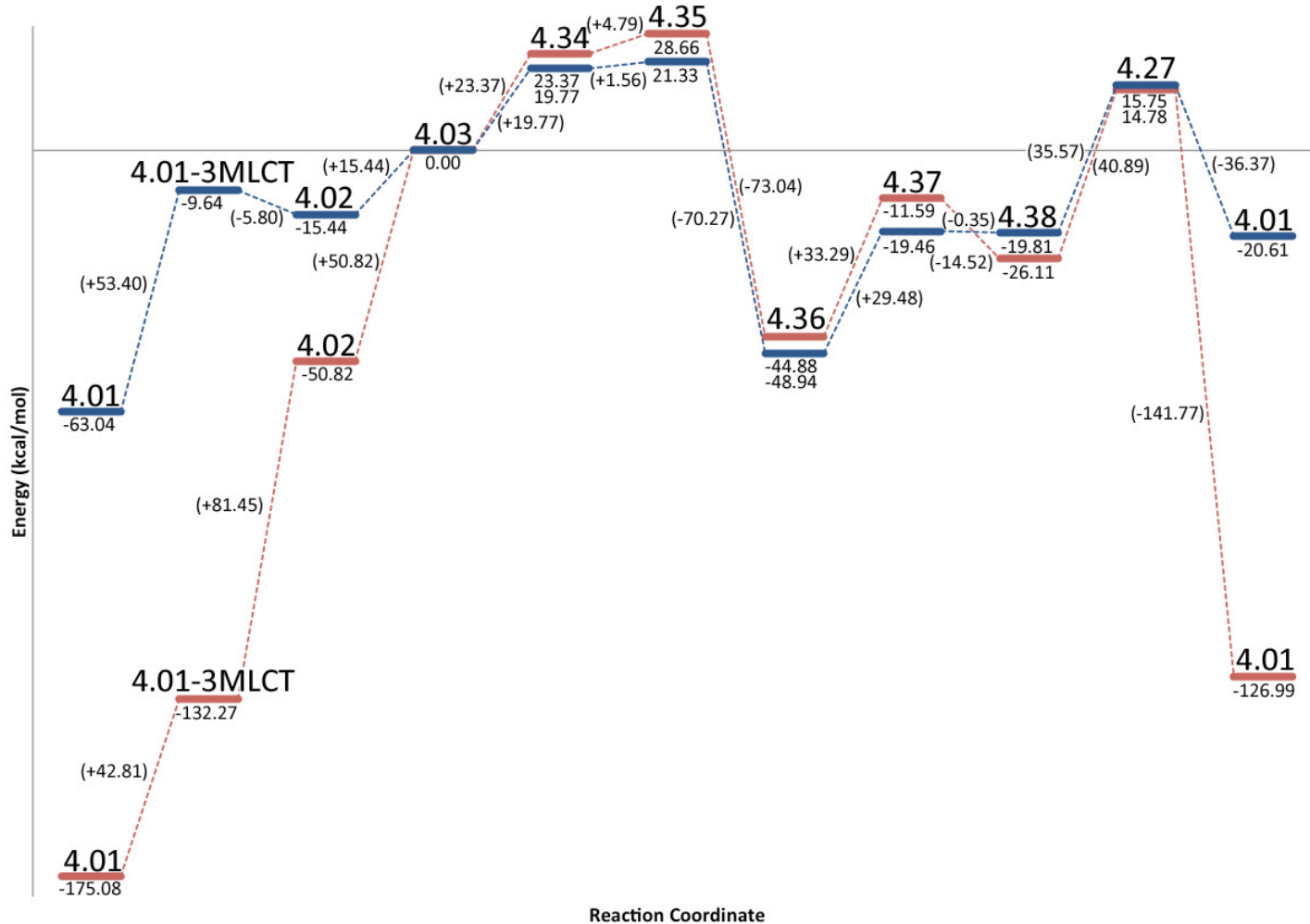


**Figure D.4** Potential Energy Surface for the planar geometry of the water-gas shift mechanistic pathway. Gas phase energies in red, DMF solvated energies in blue.

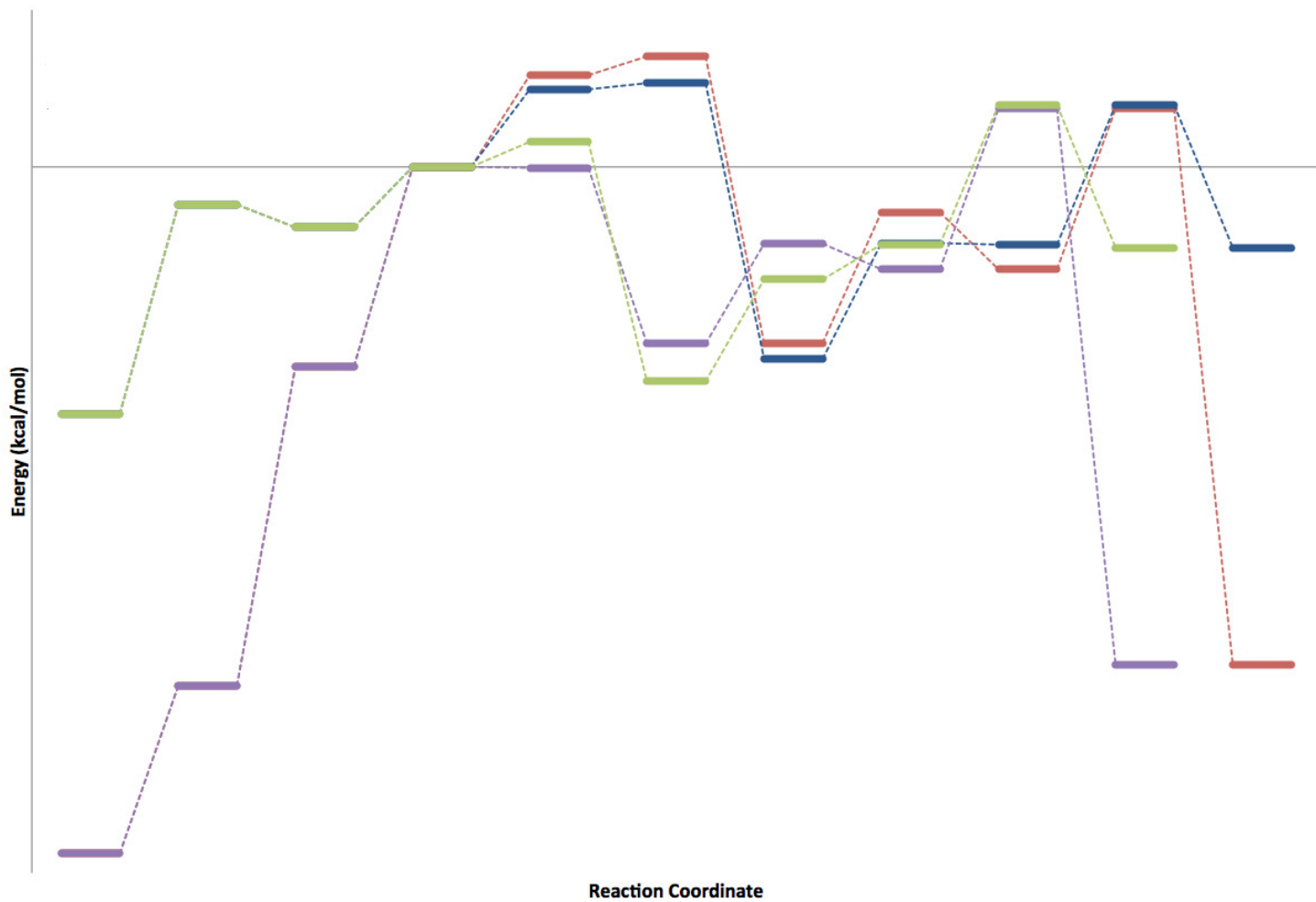


**Figure D.5** Potential Energy Surface for the two water-gas shift mechanistic pathway geometries. Axial geometry energies are shown in purple (gas phase) and green (solvated phase), and planar geometries shown in red (gas phase) and blue (solvated phase).

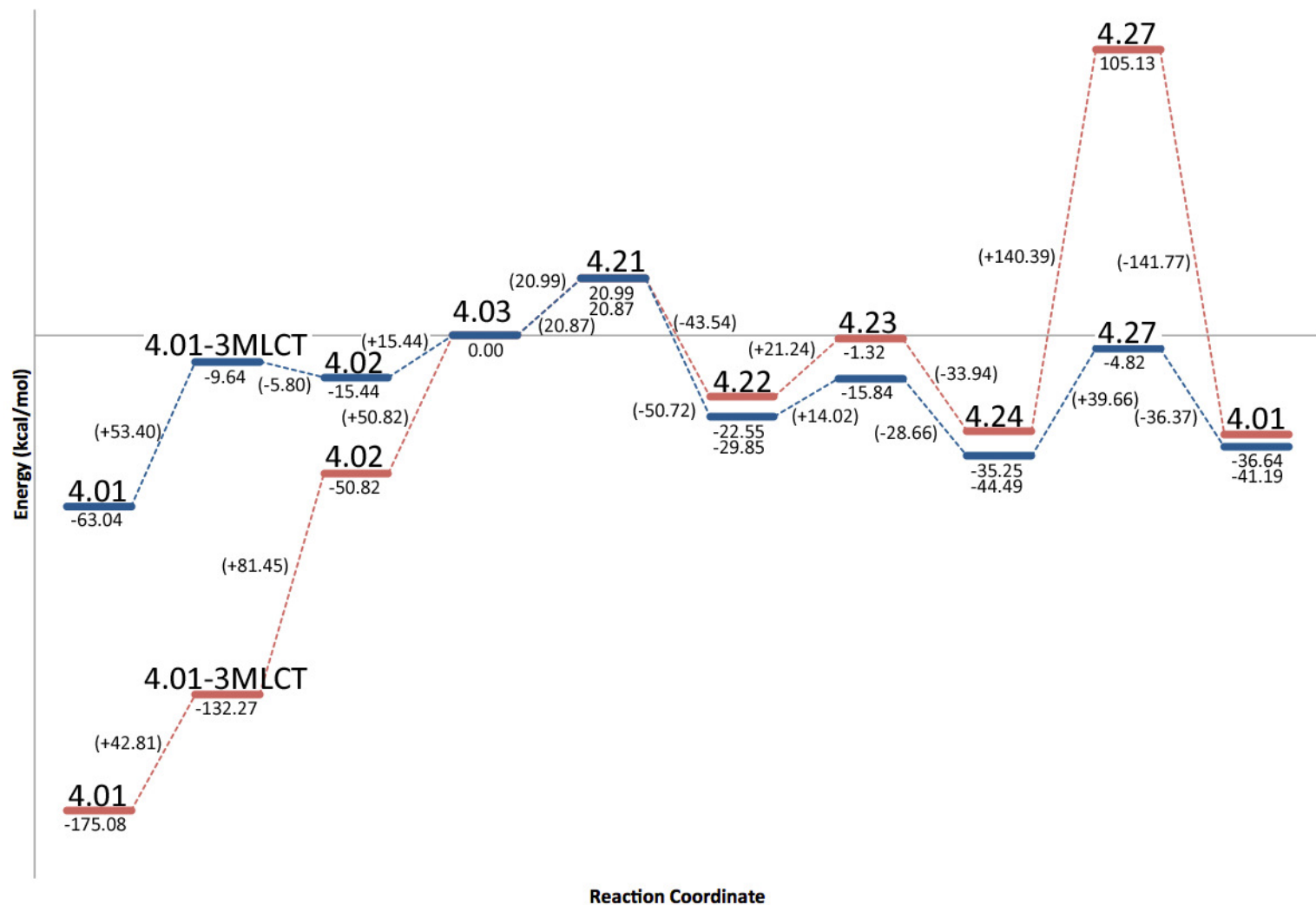


**Figure D.6** Potential Energy Surface for the formate mechanistic pathway. Gas phase energies in red, DMF solvated energies in blue.

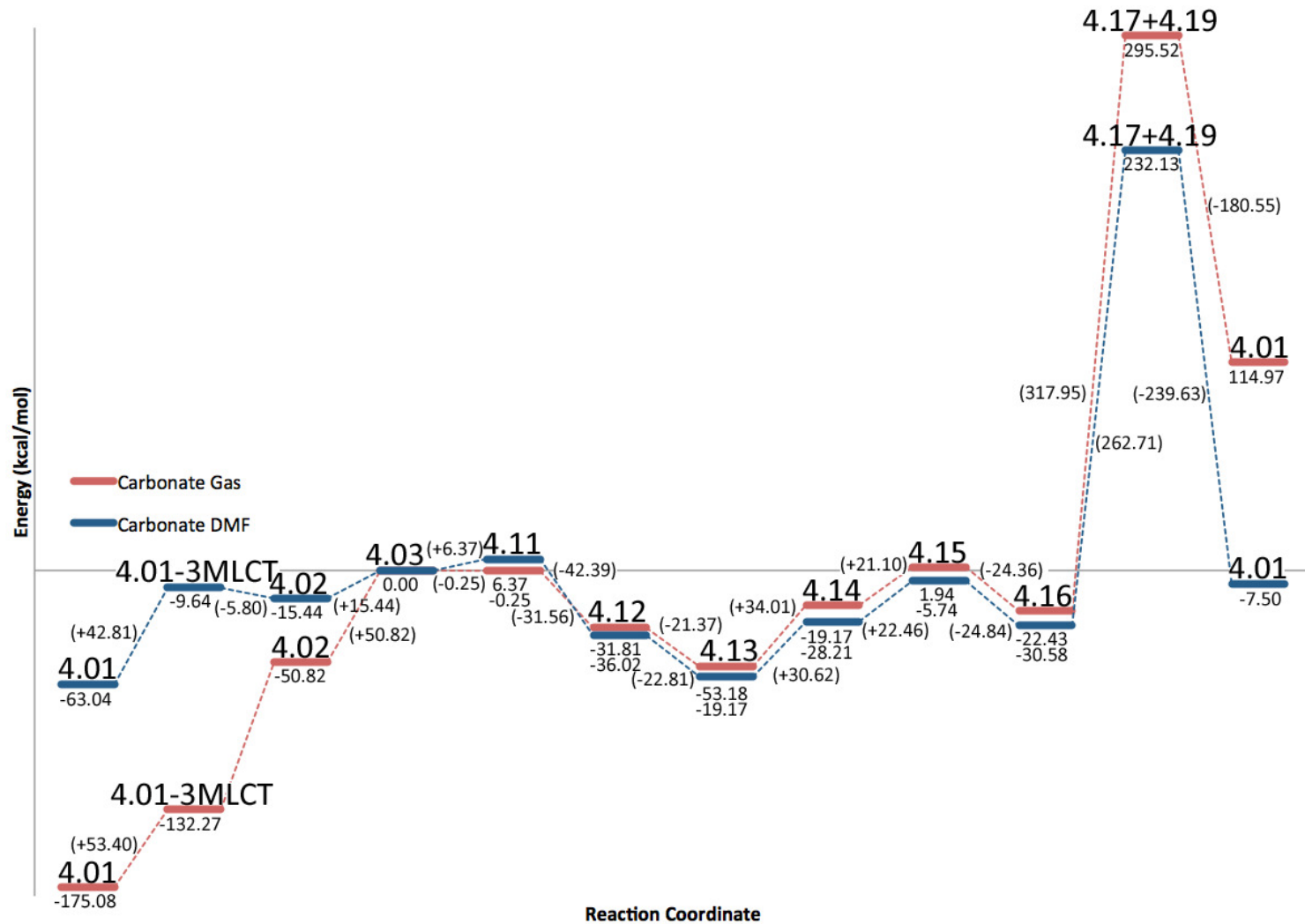


**Figure D.7** Potential Energy Surface for the bicarbonate mechanistic pathway. Gas phase energies in red, DMF solvated energies in blue.

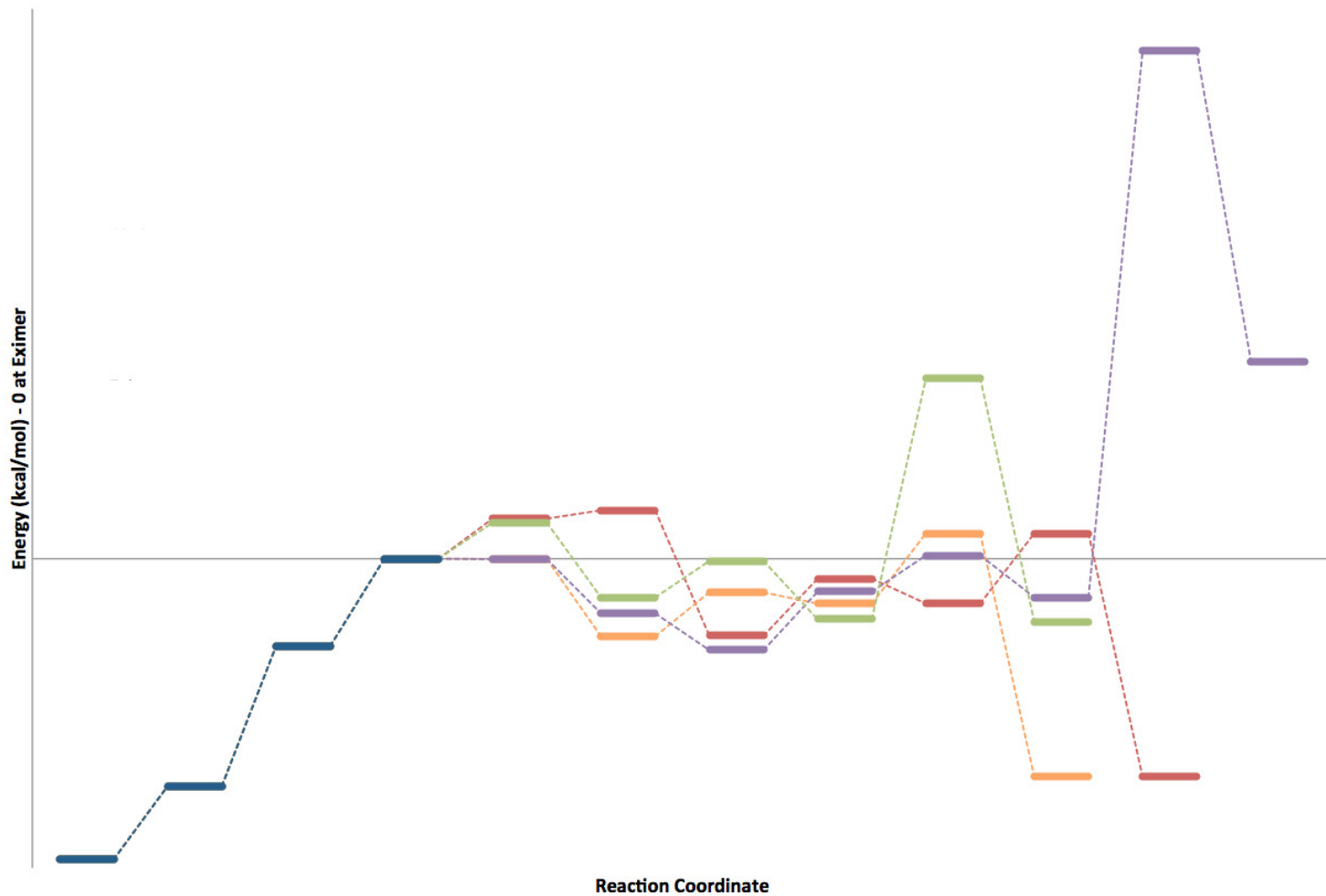


**Figure D.8** An overview of the energies of the three mechanistic pathways of photochemical  $\text{CO}_2$  reduction in gas phase. Excimer formation is shown in blue, the planar water-gas shift mechanism in red, the axial water-gas shift in orange, the bicarbonate in purple, and the formate in green.

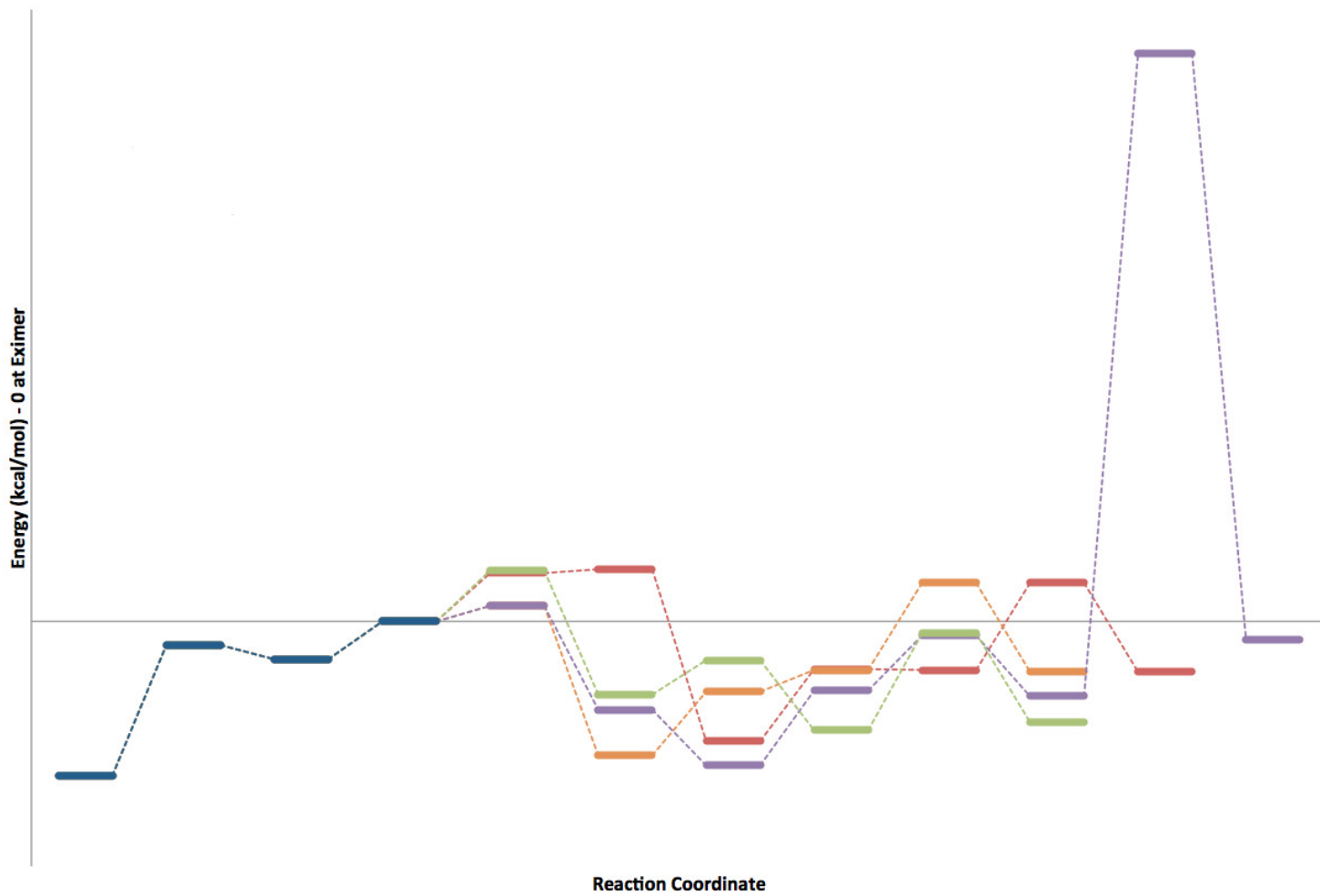


**Figure D.9** An overview of the energies of the three mechanistic pathways of photochemical CO<sub>2</sub> reduction in DMF. Excimer formation is shown in blue, the planar water-gas shift mechanism in red, the axial water-gas shift in orange, the bicarbonate in purple, and the formate in green.